2019

An Electron Paramagnetic Resonance Study Of The Magnesium Acceptor In Gallium Nitride In Different Crystal Field Environments

Ustun Robert Sunay
University of Alabama at Birmingham

AN ELECTRON PARAMAGNETIC RESONANCE STUDY OF THE MAGNESIUM ACCEPTOR IN GALLIUM NITRIDE IN DIFFERENT CRYSTAL FIELD ENVIRONMENTS

by

USTUN ROBERT SUNAY

MARY E. ZVANUT, COMMITTEE CHAIR
VLADIMIR V. FEDOROV
ROBIN D. FOLEY
EVAN R. GLASER
GARY M. GRAY
JOSEPH G. HARRISON
SERGEY B. MIROV

A DISSERTATION

Submitted to the graduate faculty of The University of Alabama at Birmingham,
in partial fulfillment of the requirements for the degree of
Doctor of Philosophy

BIRMINGHAM, ALABAMA

2019

AN ELECTRON PARAMAGNETIC RESONANCE STUDY OF THE MAGNESIUM ACCEPTOR IN GALLIUM NITRIDE IN DIFFERENT CRYSTAL FIELD ENVIRONMENTS

USTUN ROBERT SUNAY

PHYSICS

ABSTRACT

Non-uniform strain phenomena localized to Mg acceptor sites were investigated in Mg-doped GaN single crystals using electron paramagnetic resonance (EPR) spectroscopy. Samples in this study were grown either as μm-thick thin-film or mm-thick free-standing samples with the Mg concentration ranging from 3-150 $x10^{18}$ cm^{-3}. In all samples, the Mg-related EPR signal was observed but the g-factor, intensity, and lineshape anisotropy characteristics varied significantly depending on the magnitude of the bi-axial crystal field Δ_x local to the Mg acceptor. By modelling the Mg acceptor as basal atomic 2p orbitals, the angular dependent intensity could be effectively predicted in both small and large bi-axial crystal field environments. Attempts at describing the Mg acceptor as being localized to an axial nitrogen neighboring the Mg resulted in incorrect EPR g-factor and intensity angular dependent predictions for samples in small bi-axial crystal fields.

The non-uniformity of the bi-axial crystal field was investigated by measuring the EPR signal over a range of frequencies between 50-130 GHz in free-standing samples grown by vapor phase epitaxy (HVPE) samples. The dominant source of lineshape broadening was determined to be caused by non-uniform crystal field, which resulted in a distribution of unresolved g-factors, known as g-strain. Other linewidth broadening mechanisms were investigated, but all results confirm that, in the ground state, the hole

must reside on basal planes subjected to various bi-axial strains, likely attributed to their location in the crystal.

In this work, I provide experimental evidence that supports the model for the Mg acceptor as a hole on a basal site in GaN. By the application of crystal field theory, the anisotropic g-factor and intensity could be effectively understood as a parameter sensitive to the magnitude of the local bi-axial crystal field Δ_x in all GaN:Mg samples when the hole is oriented on a basal site only. Free-standing ammonothermal-grown GaN:Mg samples reveal that ionized donor sites can also result in large bi-axial crystal fields as evidenced by a reduced g-factor anisotropy.

DEDICATION

To my mother, Susan

ACKNOWLEDGEMENTS

Below is a list of people who have been paramount in making me a better human. All of you are very special to me and I will always be eternally grateful for your care and support that you have provided during my graduate career.

Mark Bentley, Leslie Denton, Martha Denton, Thomas Denton, Kathryn Ham, Kelli Lasseter, Adam Mcdermott, Adam Nored, Jeremy Peppers, Alex Skinner, Christopher Spradlin, Savannah Spencer, Laura Sunay, Meatball Parmesan Sunflower (dog), Gregory Williams, William Willoughby, and Jonathan Wright.

I also wish to extend my deep gratitude to my advisor, Dr. Zvanut, who was integral to my success as a researcher.

TABLE OF CONTENTS

Page

LIST OF TABLES

Table Page

LIST OF FIGURES

Figure Page

RESEARCH

CHAPTER 1

INTRODUCTION TO GALLIUM NITRIDE

1.1 Background and Motivation

Gallium nitride (GaN) is a semiconductor with a direct bandgap of 3.4 eV that can be altered by alloying with In or Al to achieve its most well-known application, a light emitting diode (LED) [1,2]. Developing more power-efficient optoelectronic devices is an imperative societal requirement due to an ever-increasing global demand for electrical power. GaN is pivotal in this regard, as the sole successful LED material on the market, providing significant cost and power reductions in the lighting sector. Throughout the development of LEDs, roughly every 10 years the brightness-to-LED package ratio has increased by a factor of 20 and the cost-to-brightness ratio decreases by a factor of 10 – this is known as Haitz's law. To significantly further the development of GaN LEDs and continue the trend of a more efficient device, basic research must be done to improve the understanding of the underlying fundamental processes and properties that govern GaN device functionality. The work in this document focuses on improving our understanding of the Mg acceptor– the only successful p-type dopant in GaN and a necessary component in creating LEDs.

Additionally, the high breakdown voltage, saturation velocity, and electron mobility make it an excellent material for high-power high-frequency electronic devices [3,4]. With global demands for electrical power increasing, higher efficiency devices for both cities and residents stand to save significant money on lighting. The U.S. Energy Information Administration (EIA) estimates that in 2018 the residential and commercial

sector used about 232 billion kilowatt-hours of electricity for lighting, or about 6% of the total U.S. electrical power consumption. The successful technological applications are only possible because GaN can be doped as both n-type and p-type. The former is achieved by minimizing the free carriers inherent to all current growth conditions and a controlled introduction of Si. The latter proved more challenging, but now is routinely achieved by doping GaN films with Mg – the only successful dopant that can consistently achieve p-type conductivity.

GaN, since its inception, has been plagued with severe issues that impede device performance and lifetime. Lattice and thermal expansion mismatch at the interface from hetero-epitaxy growth cause large strains that result in high dislocation densities of 10^{7}-10^{10} cm^{-2}, causing non-radiative recombination sites [5,6]. During growth, unintentional dopants (UIDs), typically Si and O, are incorporated into the GaN crystal at concentrations of 10^{16}-10^{17} cm^{-3}, which lead to n-type conductivity – making p-type conductivity harder to achieve. Regrettably, the energy level of the Mg acceptor is 150-200 meV above the valence band, resulting in a significant reduction in electrically active holes at typical operating temperatures [7,8]. Low hole mobility is also a significant concern, partially caused by doping with large impurity concentrations that increase impurity scattering and significant bi-axial crystal fields that increase the effective hole mass m_h [9]. Additionally, p-type doping efficiency also becomes reduced at Mg concentrations of ~$5x10^{19}$ cm^{-3}; this is primarily thought to be due to a higher concentration of Mg-interstitial or nitrogen vacancy donors [10,11]. For high voltage applications, it has also been seen that dislocations can migrate when the electronic device is biased, reducing device

performance and lifetime [12]. Finally, dopant incorporation has shown to be crystallographically anisotropic and, in the case of Mg, aggregated [13,14].

Despite the detrimental properties mentioned above, GaN is still the sole blue LED material and remains competitive in high-power and high-frequency electronic devices. Other impurities besides Mg have also been investigated for the purpose of finding a more suitable acceptor with a smaller ionization. For an alternative acceptor dopant to compete with Mg, the first two requirements are: having an activation energy of ~200 meV or less, and an ability to incorporate enough acceptors to compete with the 10^{16}-10^{17} cm^{-3} donors from unintentional dopants (UID). Photoluminescence characterization of Zn-doped GaN has shown features that suggest acceptor levels, but with an activation energy of about 340 meV, significantly higher than that of Mg [15]. P-type conductivity has been observed in Ca and Be ion-implanted GaN with acceptor level of about 160-170 meV and 230 meV respectively [15,16]. Unfortunately, ion-implantation incorporates dopants non-uniformly and causes additional defect states, suspected to be gallium and nitrogen vacancies and interstitials, that reduce electrical and optical device performance. Additionally, achieving p-type conductivity in Ca-doped samples requires a temperature anneal greater than 1000 ^{o}C, which significantly degrades GaN crystal quality [16,17]. Therefore, studying a means to maximize the effectiveness of the Mg dopant in GaN is a necessity in furthering the development in GaN-based electronic devices. Additionally, the effect of bi-axial crystal fields will impact two-dimensional electronic devices and significantly affect hole mobility, an issue already affecting current GaN electronics [9].

With all of the difficulties associated with GaN growth, the material possesses several desirable traits for optoelectronic applications. Firstly, the 3.4 eV band gap can be

altered by alloying GaN with other elements, Al for increasing the bandgap and In for decreasing it. The change in band gap allows the output wavelength for LEDs to be tuned. The large breakdown field of $3.5x10^6$ V cm^{-1} allows for high voltage operations, decreasing the need for power converters for voltage step-down transformers in many applications, which significantly increases power efficiency [18]. The high electron saturation velocity allows for high frequency devices, with reports of GaN-based devices being operated in the GHz range [4,19].

1.2 An Abridged History of GaN LED Progress

For most of its life, GaN has only been able to be grown heteroepitaxially, i.e. on non-native substrates. Development started in the 1960s with successful single crystalline deposition onto Al_2O_3 (sapphire) substrates [20]. Hall effect electrical measurements showed that GaN samples were strongly n-type with an electron concentration above 10^{19} cm^{-3}. This was initially attributed to a high concentration of nitrogen vacancies, but later was shown to be more likely related to the large amount of unintentional dopants and poor crystal quality. The following achievements in GaN research have led to high-brightness blue LEDs and ultimately to the 2014 Nobel prize award. By growing GaN/AlN buffer layers between the substrate and GaN active layer, residual electron concentrations were reduced to 10^{15} cm^{-3} and the surface morphology was greatly increased, mostly due to a significant reduction in dislocations [21,22]. Passivation of p-type conductivity was also seen to occur when annealing in NH_3 or hydrogen rich environments such as forming gas (N_2,H_2). To explain the passivation of Mg acceptors, hydrogen was predicted to form complexes and effectively passivate the Mg acceptor; this was later confirmed by IR

spectroscopy measurements and theoretical calculations [23]. The largest change in research interest occurred when p-type GaN was finally able to be consistently achieved - at first by Amano et al. with low-energy electron beam irradiation (LEEBI), then by Nakamura et al. via annealing in an N_2-ambient gas environment, both techniques removing H atoms from GaN:Mg crystals [24,25]. A more thorough review of GaN development has been discussed in review papers that include device development and Al/In alloying difficulties [26,27].

1.3 Growth Techniques and Properties

The majority of Mg-doped GaN (GaN:Mg) is grown using three different methods. The most common for commercial growth is metal-organic vapor phase epitaxy (MOVPE), sometimes also referred to as metal-organic chemical vapor deposition (MOCVD). Organic gas molecules, such as trimethylgallium (TMGa) and bis-cyclopentadienyl magnesium (Cp_2Mg) are passed over a hot wafer, commonly a non-native substrate such as Al_2O_3 or SiC, in a vacuum chamber and react on the surface. Growth rates for MOVPE are typically measured in μm/h with a maximum thickness of less than 10 μm with hole concentrations on the order of $5x10^{17}$ cm^{-3} [28]. Due to the hetero-epitaxial growth, reported dislocation densities are in the range of 10^7-10^9 cm^{-2} [29]. The carrier gas that is used to introduce nitrogen into the growth process, NH_3 (ammonia), results in a large hydrogen concentration, which passivates any p-type conductivity, but can be reduced with a post-growth anneal in a low hydrogen environment [25]. Other common unintentional dopants are C, Si, and O typically in the range of 10^{16}-10^{17} cm^{-3}.

For increased precision in doping concentrations, device growth, and having deposition control at the atomic level, molecular beam epitaxy (MBE) is an effective option. At "ultra-low" pressures (10^{-8} atm or lower) Ga metal sublimes while nitrogen is supplied via a plasma source to react on a substrate. To achieve higher hole concentrations, the Ga metal flow rate is modulated via a shutter and the growth method is referred to as metal-modulated epitaxy (MME) [30]. The growth rate is typically less than 1 μm/h with a film thickness of less than 1 μm but the method can incorporate a higher concentration of Mg and results in hole concentrations as high as $5x10^{18}$ cm^{-3} at room temperature. Since the growth is hetero-epitaxial, the dislocation density is similar to MOVPE; being reported at 10^{10} cm^{-2} [31]. Due to the lack of hydrogen present during crystal growth, a post-growth anneal is not required.

For many of the high-power applications to be achieved, homoepitaxial growth is preferred due to the myriad of issues from defects caused by heteroepitaxial growth, such as reduced thermal conductivity, reduced device performance and lifetime [32–35]. Furthermore, biaxial strain or crystal fields strongly affect hole mobility and lateral GaN devices, such as two-dimensional electron gas electronics [26]. For these reasons, hydride vapor phase epitaxy (HVPE) is an active area of research for GaN crystal growth. GaCl and NH_3 flow over a substrate and react to grow GaN. Growth rates at optimal conditions can be as high as 150 μm/h and can achieve mm thickness crystals. If grown heteroepitaxially, the substrate/GaN thermal expansion mismatch will accumulate stress at the interface during the cool down process, eventually result in a physical separation between the grown GaN and substrate; this process is referred to as self-separation in the literature [36]. The resulting separated GaN, referred to as "free-standing GaN", is

polished via chemical or mechanical etching. Unfortunately, one of the major disadvantages from HVPE growth is the limited Mg incorporation, with $6x10^{18}$ cm^{-3} being the highest reported concentration achieved [37].

If grown in ambient conditions, GaN will crystallize in a hexagonal wurtzite structure, referred to as w-GaN, with the space group 186 or $P6_3mc$ in Hermann-Mauguin notation with lattice constants a = b = 3.189 ± 0.003 Å and c =5.185 ± 0.002 Å [38]. A ball-and-stick model of the hexagonal cell for the crystal structure is shown in Figure 1.1 (a) and the primitive unit cell representation shown in Figure 1.1. (b) with gray colored spheres representing Ga atoms and yellow colored spheres representing N atoms. Each Ga and N atom is tetrahedrally coordinated and individually form a sublattice that is hexagonal close-packed (hcp). A polarization field arises along the crystal's c-axis due to a lack of inversion symmetry,

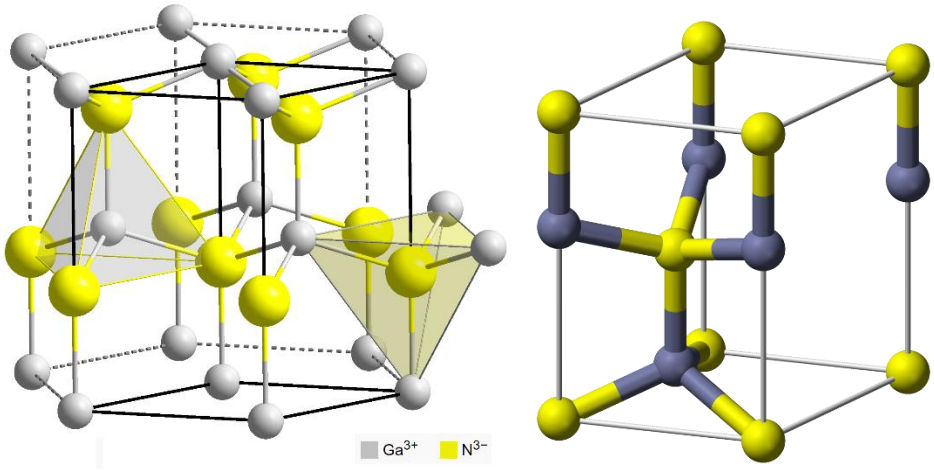

Figure 1.1. The wurtzite crystal structure of GaN showing the tetrahedral bonding for Ga (gray spheres) and N (yellow spheres) atoms with a view of the (a) hexagonal crystal symmetry and (b) primitive unit cell. Figures courtesy of Wikipedia [39].

creating an axial crystal field and causing the highest energy valence bands to become non-degenerate [40–42]. This polarization field, sometimes referred to as an axial crystal field, is often seen as a detriment in GaN devices as it creates an intrinsic depletion layer and reduces sheet carrier density control in two dimensional electron gas devices [26].

GaN can also be grown in the zincblende crystal structure, denoted as c-GaN or zb-GaN. Successfully grown c-GaN is reported to have several electronic benefits compared to w-GaN, such as a higher electron saturation velocity and no built-in polarization field. Unfortunately, many problems have been encountered that have inhibited further device development: increased complexity in growth, incompatible lattice constants between substrate and film, wurtzite inclusions, and difficulty in p-type doping [43]. The primary restriction in growth is that c-GaN is a meta-stable state and is difficult to suppress

the growth of w-GaN, the more stable crystal structure. This often results in samples that have both c-GaN and w-GaN regions.

1.4 Overview of Characterization Techniques

Various characterization techniques have been applied to determine crystal quality and electrical transport parameters of GaN films and substrates. Detailed below are some of the more common characterization techniques that are employed to effectively determine quantitative results from GaN crystal after growth. Atomic force microscopy (AFM), scanning electron microscopy (SEM), and transmission electron microscopy (TEM) have all been effectively used to determine grain size and calculate the density of several types of extended defects [44,45]. Hall effect measurements can reveal dominant

scattering mechanisms of charged carriers, determine carrier concentration, resistivity, and mobility of free carriers – for holes or electrons [10,46,47]. Many techniques have been developed to quantify crystal strain, as it has been observed to play an important role in LED device efficiency and affects charge transport characteristics [48]. A straightforward approach to quantifying crystallographic strain is performing x-ray diffraction (XRD) experiments. Depending on the type of scan, XRD has been used to determine several different manifestations of strain, including lattice parameters, axial and in-plane strain, crystal bowing, average dislocation density, layer thickness, alloying content, and mosaicity [49,50]. Raman spectroscopy has been shown to determine bulk bi-axial strain from the shift of the E_2^2 vibrational mode and relative free-carrier concentration from the A_1(LO) mode [51,52].

The above-mentioned characterization techniques focus mainly on extended defects and their effect on bulk crystal properties but point defects in GaN have also been observed and quantified. Secondary ion mass spectrometry (SIMS) standards have been developed for GaN to accurately determine atomic concentrations of common dopants, e.g. Mg, O, Si, C, as a function of depth within the sample [53]. SIMS, however, cannot differentiate between different atomic charge states or determine the mechanism of dopant incorporation, e.g. substitutional or interstitial. Since near-band edge optical transitions are well understood in GaN, low temperature photoluminescence (PL) spectroscopy can provide extremely valuable information about point defects. Many crystal quality parameters, such as strain, can be extracted by inspecting the PL from optical transitions related to band-to-defects or acceptor/donor bound excitons [54]. Finally, electron paramagnetic resonance (EPR) techniques have been shown to be an effective tool for

determining the local structures of many impurities and their charge states in GaN, such as Fe^{3+} and Mn^{2+}. The wavefunction localization for the neutral Mg acceptor in GaN, however, has eluded experimental scientists.

1.5 Overview of Point Defect Characterization in GaN

On the journey to achieving GaN-based LEDs, many different point defects have been studied as a potential pathway to understand in more detail their impact on the electrical and optical properties of GaN. In this section, I briefly discuss some of the more heavily studied point defects and their structures in GaN. For a more thorough review, PL characterization from Reshchikov et al., first-principle calculations from C.G. Van de Walle et al., and a general overview by M.O. Manasreh provide a more detailed account of point defects in GaN [54–56]. In most unintentionally doped and intentionally doped n-type GaN samples, the photoluminescence spectrum contains a yellow band emission that peaks around 2.25 eV, referred to as YL in the literature. For decades, the dominant mechanism for the observed YL has been heavily debated [54].

1.5.1 Native defects

Initially expected to be the dominant source of n-type conductivity, direct identification of isolated nitrogen vacancies ,V_N, have continued to evade spectroscopists. Density functional theory (DFT) computations predict a low formation energy for V_N, and that nitrogen vacancies should be present in GaN at large concentrations, but has yet to be directly observed [57]. However, nitrogen vacancy complexes, such as Mg_{Ga}-V_N, have been calculated to be the origin of many PL emission peaks [54]. Gallium vacancies, V_{Ga}, act as acceptor-like defects with a low formation energy in n-type GaN and have been

detected via positron annihilation spectroscopy (PAS) [58]. V_{Ga} is also thought to be one of the defects that result in a yellow-band luminescence in n-type GaN [54]. Additionally, several authors have studied electron-irradiated n-type GaN and observed a wide variety of defects which include Ga-O complex, Ga interstitial and a trapped Ga or N vacancy [59,60]. Recent frequency-dependent EPR measurements have also identified the interstitial N-N [61].

1.5.2 Defects in n-type GaN

Finding a suitable dopant to make n-type GaN has, historically, been a much easier task than the search for efficient p-type doping. Both O_N and Si_{Ga} have been shown to be effective donors with their activation eneries being ~14 and 35 meV, respectively, below the conduction band [62]. Additionally, the small formation energies determined from DFT calculations compared to other native defects allow for high concentration of Si_{Ga} or O_N without issues of self-compensation mechanisms [11,63]. Thorough EPR studies of thin-film GaN:Si have been carried out by Carlos et al., investigating the effects of strain and donor concentrations and the surrounding Si local environment [64]. Bulk HVPE GaN:Si has also been shown to form a defect band at electron concentrations of 1.6×10^{18} cm^{-3} and determined that transverse spin relaxation (T_2) is the dominant spin relaxation mechanism [65].

1.5.3 Transition metals

For some device applications, such as high-electron-mobility transistors (HEMTs), creating an electrically insulating layer is required to maintain a two-dimensional electron gas. Since unintentionally doped GaN is n-type, transition metals (TMs) have been

effective in compensating donors in the material and reducing conductivity. Additionally, TMs are often a common trace impurity in many semiconducting materials and their effect on optical and electrical properties is needed. To date, all experimental results indicate that transition metal impurities substitute for the Ga ion in GaN, with computational formation energy diagrams confirming TM_{Ga} is small compared to other configurations [66,67]. The TM ions give three electrons to bonds and the remaining valence electrons stay well localized. For many of the TM impurities in GaN, defect levels are formed deep in the bandgap, reducing the Fermi level and creating a more electrically insulating material. Since only unpaired spin systems can be paramagnetic, i.e. $S \neq 0$, only some charge state of a TM will be EPR active. Several transition metal and rare earth metal charge states in GaN have been observed in EPR, such as: Fe^{3+}, Mn^{2+}, and Er^{3+} [68–70]. Concern should be placed on transition metal incorporation in GaN-based LEDs, as Fe^{3+} has been shown to be an effective Shockley-Read-Hall recombination center and even trace amounts severely reduce the amount of light emitted [66,71].

1.5.4 Hydrogen-related defects

Hydrogen has become a heavily studied impurity in GaN, as its interaction in Mg-doped samples is a death knell for achieving p-type conductivity. Direct experimental observations of H-related defects are concentrated mainly on vibrational spectroscopy. Initial studies characterized the Mg-H complex [72]. N isochronal and isothermal annealing studies have been extensive in determining activation energies in Mg-doped GaN samples via electrical measurements [73,74]. Gallium vacancy complexes have also been observed to be “decorated” with a various number of H atoms ($V_{Ga}H$, $V_{Ga}H_2$, $V_{Ga}H_3$) [75].

1.6 Overview of the Mg Acceptor in GaN

Despite the importance attributed to the Mg dopant, most of the fundamental structural information about the acceptor is provided by computational results. By using density functional theory (DFT), a computational quantum mechanical modeling technique, scientists can predict the formation energies and electrical properties of defects in crystals [55,57,76]. All results indicate that Mg substituting for Ga has the lowest energy formation, denoted by Mg_{Ga} and visualized by the schematic in Figure 1.2 (a), but that there are three acceptor transition level states with distinct physical localizations within the crystal [77]. Two of these states have the hole residing mostly on a neighboring nitrogen atom, with the difference being that one state is localized mostly on an axial nitrogen, labelled as A in Figure 1.2 (b), and the other is localized on one of three neighboring basal nitrogen atoms, labelled as B in Figure 1.2 (b). The third state, referred to as the shallow transient state (STS), is delocalized along the $[11\bar{2}0]$ basal nitrogen atoms. With current computational accuracies, it is not possible to determine the ground state between these three distinctly different states as the energy differences are less than 20 meV.

Typically, the detailed structure of an impurity may be experimentally probed by magnetic resonance that can determine the unpaired spin distribution through examination of the electron-nuclear hyperfine interaction. Unfortunately, such information is unavailable for Mg in GaN, likely due to spectral broadening caused by the 100% abundant nuclear spins of Ga and N and sample strain. It should be noted that magnetic resonance

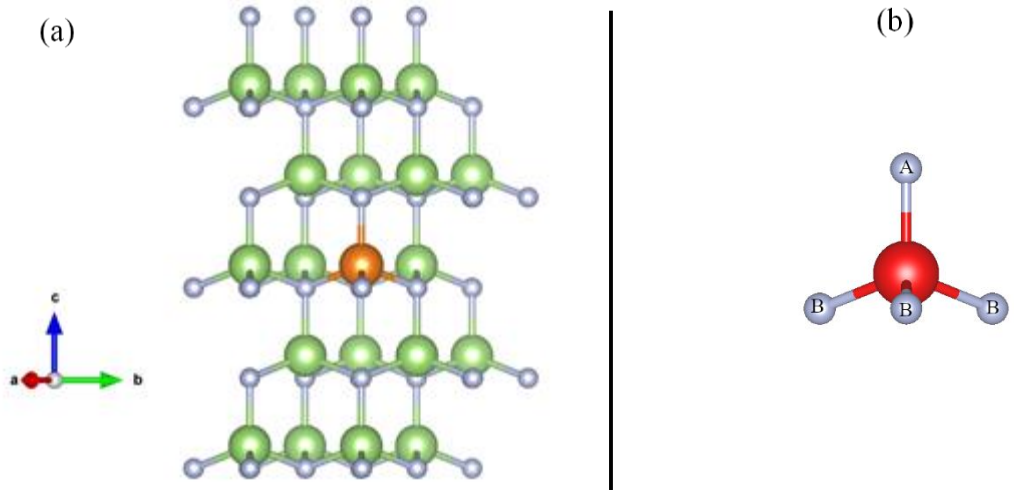

Figure 1.2. (a) Schematic of Mg (orange sphere) substituting at a Ga (green) site surrounded by 4 N (silver) atoms in hexagonal GaN. a, b, and c are the hexagonal crystal axes with |a|=|b|. The basal plane, mentioned in the text, is the crystal ab plane. The axial nitrogen is a nearest neighbor to Mg lying along the c-axis; the basal nitrogen are nearest neighbors in the basal plane. (b) The isolated Mg_{Ga} atom with an axial (A) and three basal (B) N atoms.

can detect only the uncompensated, or neutral **Mg acceptor Mg^0**. To date, the only magnetic spectroscopic information about Mg^0 is the g-factor, a parameter derived from the interaction of the paramagnetic electron with the surrounding crystal. Nevertheless, a magnetic resonance study of heteroepitaxial films, combined with SIMS and PL, convincingly associated an isotropic ~15 mT peak-to-peak broad (ΔB_{pp}) resonance at 24 GHz having $g_{\parallel} = 2.08$ and $g_{\perp} = 2.00$ with the Mg acceptor [78–80]. The 1.6 K PL spectra of Mg-doped GaN thin-films revealed a broad emission centered at 3.0 eV. By performing optically detected magnetic resonance (ODMR) on all PL emission processes from 2.73- 3.02 eV, a paramagnetic defect with $g_{\parallel} = 2.080 \pm 0.01$ and $g_{\perp} = 2.000 \pm 0.01$ was observed for exclusively Mg-doped GaN.

1.7 Motivation for Research

Currently, research in GaN leaves the ground state of the uncompensated Mg acceptor as a controversial topic. Initial experimental work by Alves et al. and computational work by Lyons et al. predicted that the hole was localized on an axial N neighbor or delocalized equally to all four N neighbors [81,82]. Later, experimental ODMR measurements by Glaser et al. and Aliev et al. showed that only a basal-oriented hole could explain both low and high basal-strain samples [83,84]. Adding to the complication, more recent computational papers reveal three potential candidates for the ground state of uncompensated Mg [77]. Without a consensus to the nature of the Mg acceptor ground state, it is difficult to advance p-type properties in GaN – with Mg being the only successful p-type dopant in GaN. Therefore, the motivation of this work is to provide additional evidence for the "true" ground state of Mg.

Although computational DFT calculations cannot determine the ground state from three possible options, analysis from the EPR experiments in this dissertation require that the hole be mostly localized on basal atoms. The model of the Mg acceptor derived from experiment thus far states that the hole prefers a basal localization and is subject to the non-uniform strain created by the crystal growth conditions. However, the model is based solely on one parameter, the EPR g-factor. Another feature of the EPR that can be analyzed is the intensity. A comparison of the EPR intensity with that predicted by the crystal field model was limited in the past by the small variation observed in the spectral intensity of heteroepitaxial films and low signal-to-noise ratio observed for homoepitaxial films. However, the significantly improved signal-to-noise ratio and highly anisotropic spectral intensity provided by thick free-standing Mg-doped crystals provides an opportunity to test

the crystal field model and the important conclusion regarding the localization and symmetry of the Mg hole.

In addition to probing the local symmetry of the Mg acceptor, the non-uniformity of the basal crystal field in free-standing HVPE samples can be investigated. Although basal strain has been investigated for bulk GaN, as reported by Freitas et al., little is known about the local environment surrounding the Mg acceptor [85]. Reshchikov et al. reported "potential fluctuations" in HVPE free-standing GaN:Mg samples from PL measurements, stating that the non-uniformity of the crystal fields alter the ultraviolet luminescence (UV) band maximum [86]. Glaser et al. observed the neutral Mg in homoepitaxial thin-films via ODMR and described the signal to have a strong angular dependent lineshape [83]. Zvanut et al. were able to describe the angular dependent lineshape of the Mg-related EPR signal by a distribution of paramagnetic centers with differing g-factors caused by a non-uniform basal crystal field around the Mg acceptor [87]. In this work, we investigate these claims of a non-uniform basal crystal field via frequency-dependent EPR measurements. We also examine the crystal bowing and EPR spin-relaxation impact on the EPR frequency-dependent linewidth.

The previously mentioned studies are based on the premise that the magnitude of local basal crystal fields influence several EPR characteristics of the uncompensated Mg acceptor. By investigating Mg^0 in a wide variety of different local environments, we can compare EPR experimental results to the characteristics predicted in a basal-N model. For example, by alloying GaN with In or Al, many of the bulk crystalline properties have been observed to change in XRD, Raman, and PL. To investigate the impact of alloying and assign a physical connection to the characteristics of the resulting EPR parameters,

MOVPE grown $Al_xGa_{1-x}N$ samples were studied with x ranging from x = 0 to x = 0.28. Also, different mechanisms for a strong basal crystal field on Mg^0 can be studied in p-type ammonothermal GaN:Mg samples, which are measured to have a small bi-axial strain but predicted to contain a large crystal field due to a high concentration of compensated donor sites.

1.8 Overview of Chapters

Progress in doping-related phenomena, such as increasing p-type electrical properties in GaN, often depend on diagnostic tools for assessing the presence and properties of dopants. Most techniques that characterize GaN:Mg determine properties of the bulk material but are unable to provide specific information about the local environment surrounding the Mg acceptor. Further development of a Mg^0 model will benefit from the quantitative data that can be extracted from EPR spectroscopy measurements and assist materials scientists in further characterization of their grown crystals.

In this work I show novel experiments and calculations that reveal additional information about the local symmetry of the Mg acceptor. In order to interpret the results from the conducted research, Chapter 2 gives an introduction to the experimental techniques used, mostly focusing on electron paramagnetic resonance (EPR). The theory for calculating an effective g-factor for a given paramagnetic system is discussed along with common EPR broadening mechanisms. In section 2.7, more specific arguments are made against the Mg hole localized to an axial hole.

Chapter 3 provides information specifying experimental parameters. All samples used in the study are described and some of their basic crystal properties are presented in

Table 3.1. The EPR experimental setup for both X-band and frequency-dependent measurements are described, along with XRD and Raman measurements.

Chapter 4 presents and discusses the findings of all the experimental research conducted. A crystal field model is introduced and applied to the samples in this study to understand the Mg acceptor in different bi-axial strain environments [84]. I also determine the crystal quality impact on EPR experimental results, specifically the c-axis crystal curvature on the EPR frequency-dependent linewidth. Lastly, I introduce temperature-dependent EPR linewidth data and discuss potential explanations that would be consistent with the crystal field model. The work presented contributes more evidence that the Mg-acceptor is localized to a basal plane in GaN.

Chapter 5 summarizes the results and discusses the physical implications of the experiments. I also suggest additional experiments which could be done if the appropriate resources become available.

.

CHAPTER 2

EXPERIMENTAL TECHNIQUES

2.1 EPR Spectroscopy Basic Applications

The most common conversations I have at conferences and with colleagues is "I don't understand EPR spectra at all. Why does the y-axis have no units? What does each peak in a spectra mean? Why are you always so interested in this g-factor parameter and what does it mean?". Throughout this section I will attempt to answer these questions and provide the appropriate amount of information required to interpret my findings reported in Chapter 4.

Electron paramagnetic resonance (EPR) spectroscopy is a tool for studying systems with non-zero spin angular momentum, being commonly employed in biology, chemistry, and physics. The main appeal of EPR is its ability to probe the local environment of a center, leading to very specific insight into local interactions and determination of spin density on atomic sites. Understanding EPR spectra often requires an analysis of the energy levels for a given system determined by appropriate modeling from the surrounding environment. For example, a nuclear spin $I \neq 0$ near the paramagnetic center can cause additional spectral peaks, or the local symmetry of the environment surrounding the paramagnetic center will impact the angular dependence in EPR spectra. Another important property of EPR spectra is that the intensity of a signal is directly proportional to the total number of paramagnetic centers in the sample, so that total number and average concentrations of a specific defect can be determined. The accuracy of determining

concentration varies depending on several variables, but for Mg in GaN the error is approximately 50%. Due to the quantitative nature of the spectroscopy, EPR is commonly used for species identification and characterization of point defects. Below is a discussion of the simplest case that results in an EPR signal, a single electron exposed to an external magnetic field. From there we will build up to what is required to effectively understand my research, but in no way is a comprehensive examination on the topic of EPR.

2.2 Zeeman Effect for S = ½ System

An unpaired electron has a net spin magnetic dipole moment $\boldsymbol{\mu}_s = -g_e(e/2m)\,\boldsymbol{S}$ with a corresponding spin quantum number S=½. When exposed to an external magnetic field B_o, the magnetic moment from the electron aligns itself either parallel (m_s=½) or anti-parallel (m_s=-½) to the direction of the field. The energies of the two discrete states are quantized by the Zeeman interaction term specified by the electron magnetic moment $\boldsymbol{\mu_s} = \mu_B g_e \boldsymbol{S}$ and external magnetic field **B**, $H = -\boldsymbol{\mu}_s \cdot \boldsymbol{B}$ with eigenvalues

$$E = \mu_B g_e B_o m_s \tag{2.1}$$

where μ_B is the Bohr magneton g_e is the g-factor for a free electron which is approximately 2.0023, and B_o is the applied external magnetic field [88]. As the external magnetic field increases in magnitude, the energy differences between the two spin states linearly increases as shown by plotting Eq. (2.1) for $m_s = \pm ½$ in Figure 2.1 (a). An unpaired electron can transition between the parallel and anti-parallel states by the absorption of a

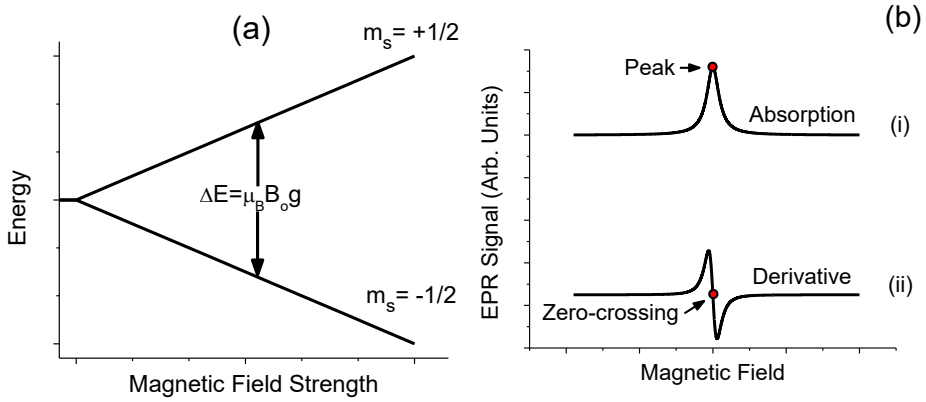

Figure 2.1. (a) The energy splitting between spin states due to the Zeeman effect and the (b) resulting (i) absorption and (ii) derivative EPR spectra for a S=1/2 system. B_o is the magnetic field at peak of the EPR absorption or zero crossing for a derivative scan.

photon in the microwave region when the energy difference between states ΔE is equal to the photon energy, i.e.

$$\Delta E = \mu_B g_e B_o m_s = hv \qquad (2.2)$$

where h is Planck's constant and v is the frequency related to the photon. Eq. 2.2 is often referred to as the "EPR resonance equation". For a free electron, this spin transition occurs at a magnetic field of about 3350 Gauss when using a frequency source of 9.5 GHz.

The corresponding EPR absorption spectrum for a transition is shown in (i) of Figure 2.1 (b). The magnetic field B_o represents where the peak of the absorption occurs, or, in the case of a derivative mode spectrum, shown in Figure 2.1 (b-ii), the zero-crossing. The majority of EPR spectrometers don't measure the absorption *A* of microwaves, but instead measure the change in microwave absorption with respect to magnetic field (*dA/dB*)

by means of phase sensitive detection (PSD). To quickly summarize the appeal of PSD, by modulating the static magnetic field at a specified reference frequency Ω_o (typically 100 KHz in EPR), the response of the system can be filtered at the reference frequency Ω_o. By using PSD, the signal-to-noise ratio is significantly increased, and the derivative of the microwave absorption is recorded as seen in Fig. 2 (b-ii). A more mathematical and detailed explanation can be found by D.P. Blair and P.H. Sydenham [89].

2.3 The EPR g-factor

For an unpaired electron at a defect in a crystal, the local environment induces interaction terms into the Hamiltonian. The inclusion of a strong local magnetic field will alter the g-factor away from $g = g_e$ and the symmetry of those fields can be reflected in the EPR angular dependence. To describe these local fields, we start by expressing the complete Hamiltonian of the defect for a S = 1/2 spin system with no nuclear hyperfine interactions

$$H = H_{KE} + H_{ee} + H_{CF} + H_{SO} + H_B \tag{2.3a}$$

$$= H_o + H'$$

$$H_o = H_{KE} + H_{en} + H_{ee} \tag{2.3b}$$

$$H' = H_{CF} + H_{SO} + H_B \tag{2.3c}$$

where H_{KE} is the kinetic energy, H_{ee} is the interaction term from other electrons orbiting the same nucleus, H_{CF} is the crystal field interaction, H_{SO} is the spin-orbit coupling, and H_B is the Zeeman interaction term which arises in the presence of an external magnetic field

specified in Eq. 2.1. The first three terms are typically the starting point for guessing a good wave-function basis set to describe the defect. The second set of terms, H_{CF}, H_{SO}, and H_B are significantly weaker interactions. In terms of energy magnitude, the first three terms are typically of the order of tens to hundreds eV depending on the system, while all subsequent terms are usually less than 0.1 eV. Since there is such a large difference in interaction energy, we will let the rest of the terms in H′ be treated by perturbation theory using the energies and wavefunctions of H_o. The term H_{CF} is the crystal field or "ligand field" term that describes the coulombic interaction of the defect with nearby ions approximated as point charges. Since the exact form of H_{CF} is dependent on the placement of the point charge "ligands", H_{CF} is therefore entirely dependent on the local point symmetry of the defect. For the neutral Mg acceptor defect, the Mg substitutes a Ga site and is denoted as Mg_{Ga}. H_{CF} for Mg_{Ga} has tetrahedral symmetry with a trigonal distortion along the c-axis. A theorem by Stevens states that the total momentum operators $\hat{J}_x$, $\hat{J}_y$, and $\hat{J}_z$ can be used to express the radial component of the crystal field state energies, which are generally written as a sum of Stevens' operators $\hat{O}_k^q$ [90,91]. For ions in crystal field of intermediate strength, i.e. when the crystal field energy exceeds the spin-orbit coupling energy, then the total momentum operators are replaced by angular momentum operators $\hat{J}_i \rightarrow \hat{L}_i$. In GaN, the ground state of Mg^0 will be S = ½ and we can write the relevant crystal field operators as

$$H_{CF} = -\frac{2}{3}B_4\hat{O}_4^0 + B_2^0\hat{O}_4^0 \tag{2.4a}$$

$$H_{CF} = \Delta_z\left(\hat{L}_z^2 - L(L+1)/3\right) \quad (2.4b)$$

where the first term in Eq. 2.4 (a) is the cubic crystal field from tetrahedral symmetry and the second term is the trigonal crystal field. For a S = ½ spin system, Eq. 2.4 (a) simplifies to Eq. 2.4 (b). The Hamiltonian terms for the spin-orbit interaction H_{SO} and interaction with an external magnetic field H_B can be written as

$$H_{SO} = \lambda \boldsymbol{L} \cdot \boldsymbol{S} \quad (2.5a)$$

$$H_B = \mu_B \boldsymbol{B}^T \cdot (g_e \boldsymbol{S} + g_l \boldsymbol{L}) \quad (2.5b)$$

Where the first term in Eq. 2.5 (b) is the Zeeman interaction term for an electron's spin state, and the second term describes the magnetic interaction for the orbital momentum. The variable g_l is referred to as the covalency or orbital reduction factor and for the free electron case is equal to unity. In molecules or crystals, g_l can be reduced by an increased molecular orbital formation and can be used as a measure for wavefunction delocalization [92]. Later, in section 4.8, it will be discussed how g_l can also be reduced through the dynamic Jahn-Teller effect.

2.3.1 The non-degenerate case

The intrinsic spin angular momentum of a free electron that characterizes its magnetic moment is related by a g-factor of 2.00232. For free atoms, determining the magnetic moment requires the inclusion of an orbital momentum contribution and application of the Landé g-factor formula. In molecules and crystals, however, the

unperturbed ground state of an orbitally non-degenerate spin system will have zero angular momentum. By including the Hamiltonian interactions of 2.5 (a) and 2.5 (b), the ground state will be admixed with a small amount excited states.

At this point, it is mathematically convenient to redefine the g-factor from a scalar to a 3x3 matrix, with the interactions of local fields transferred to $\overleftrightarrow{\boldsymbol{g}}$ and wavefunctions being "effective" spin states. The Hamiltonian is now expressed only as a spin Hamiltonian

$$H = \mu_B \mathbf{B}^{\boldsymbol{T}} \cdot \overleftrightarrow{\mathbf{g}} \cdot \mathbf{S} \tag{2.6a}$$

$$\overleftrightarrow{\mathbf{g}} = g_e \overleftrightarrow{\mathbb{I}} + 2\lambda \overleftrightarrow{\boldsymbol{\Lambda}} \tag{2.6b}$$

$$\Lambda_{ij} = \sum_{n \neq G} \frac{\langle G | \hat{L}_i | n \rangle \langle n | \hat{L}_j | G \rangle}{E_n^{(0)} - E_G^{(0)}} \tag{2.6c}$$

Where $\overleftrightarrow{\mathbb{I}}$ is the 3x3 identity matrix, $|G\rangle$ and $|n\rangle$ are the ground and excited states respectively, and $E_i^{(0)}$ is the unperturbed energy. In this viewpoint, the g-factor matrix elements are now a measure of the linear response between the energy of an effective spin state and the external magnetic field. There will exist a coordinate system where the g-factor matrix is diagonal, which is referred to as the defect coordinate system, with principle values g_x, g_y, and g_z. Now for any given orientation between the defect coordinate system and the applied magnetic field, the observed g-factor can be expressed as

$$g^2 = g_X^2 \cos^2 \theta_{B,X} + g_Y^2 \cos^2 \theta_{B,Y} + g_Z^2 \cos^2 \theta_{B,Z} \tag{2.7}$$

Where $\theta_{B,x}$, $\theta_{B,y}$, and $\theta_{B,z}$ are the angles between the defect axis and static magnetic field. Sometimes, the paramagnetic g-factor eigenvectors will coincide with the symmetry of the crystal field from the host crystal. Experimental results for Mg^0 in GaN have revealed that, to date, the crystal c-axis is the local symmetry axis; this results in two principle g-factors having the same value. In literature this is traditionally chosen to be g_x and g_y. In the case of axial symmetry systems, the principle g-factors are now denoted by $g_x = g_y = g_\perp$ and $g_z = g_\parallel$. To accurately obtain values for $g_\parallel$ and $g_\perp$, the sample should be rotated in a plane containing the symmetry axis, which is the c-axis for GaN:Mg. The directions between the magnetic field and defect axes can now be expressed as

$$g^2 = g_\perp^2 \sin^2\theta + g_\parallel^2 \cos^2\theta \tag{2.8}$$

where θ is the angle between the c-axis and the static magnetic field. Experimentalists will add an offset angle, i.e. $\theta \rightarrow \theta+\theta_o$, to account for error in initial loading of the sample into the cavity, giving an improved fitting for $g_\parallel$ and $g_\perp$.

To give an example of the physical manifestations from Eq. 2.8, let us say that a defect with c-axis symmetry in a single crystal is measured in an EPR spectrometer. We rotate the sample to change the angle between the c-axis and the external magnetic field **B** θ as shown in Figure 2.2 (a). With each unique angle of θ, the zero-crossing B_o will correspond to an effective g-factor by rearrangement of Eq. 2.2

$$g(\theta) = \frac{h\nu}{\mu_B B_o(\theta)} \tag{2.9}$$

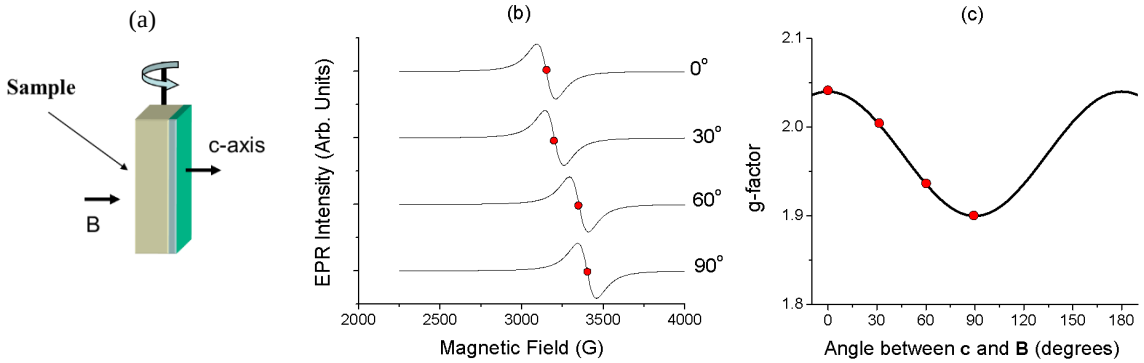

Figure 2.2. (a) Schematic of how samples are rotated for EPR angular dependent measurements. (b) Example stacked EPR spectra taken at different orientations between the crystal c axis and the external magnetic field B. The zero crossing B_o from each spectrum is highlighted by a red circle and (c) the corresponding effective g factor is determined by application of Eq. 2.9.

The corresponding spectra are plotted in Figure 2.2 (b) and the extracted g-factors are plotted as red circles in Figure 2.2 (c). We can now quantify the anisotropy of the g-factor defect by fitting the parameters $g_{\parallel}$ and $g_{\perp}$ from Eq. 2.8 to the experimental g-factors. In practice, verifying the symmetry of a defect requires rotation in three unique planes [88].

Examples of g-factor calculations starting from crystal field symmetries are shown in many textbooks [88,91]. Wertz and Bolton specifically deals with more complicated cases, such as orbital degenerate ground states and rare earth ions, where the spin-orbit coupling term is stronger than crystal field splitting, e.g. for rare-earth elements and the total angular momentum quantum number J is more appropriate than L or S to use in crystal field and Zeeman effect operators.

2.4 The EPR Intensity

By comparing the intensity of a standard with a known number of spins to a researcher's unknown sample, the number of spins can be calculated [88]. In practice, the intensity of a given paramagnetic center is the value of the double integral of an EPR

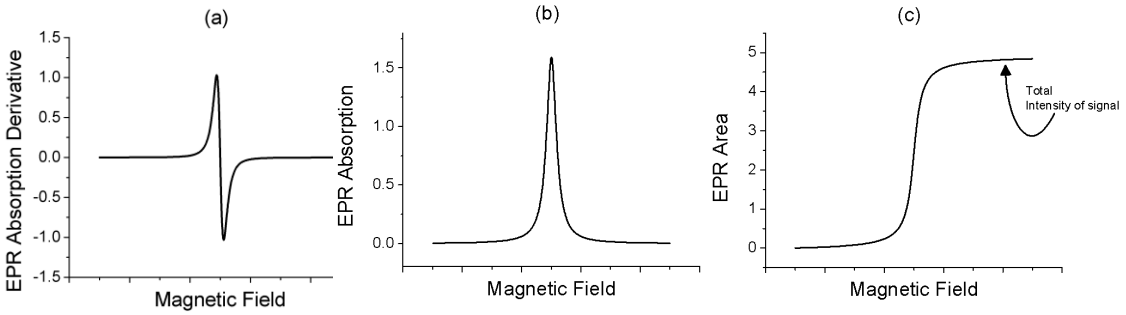

Figure 2.3. (a) An example EPR spectra taken in derivative mode, (b) its corresponding integral with respect to the magnetic field strength B, and (c) the second integral with respect to B.

spectrum as shown in Figure 2.3. Typically, most of the error from calculating EPR concentrations comes from numerical intensity errors, and, on thin-films, accurate volume calculations. For the case of transitions with a Lorentzian lineshape, which best describes the Mg-related EPR signal in thin-films, the area under the curve converges slowly, introducing a 10% error when taking integration limits $\pm 10\Delta B_{pp}$ where ΔB_{pp} is the peak-to-peak linewidth of a given transition [93]. In the case of free-standing GaN:Mg samples, it will be shown in the results and discussion that the EPR intensity is angular dependent and will create additional error into concentration calculations.

2.5 Linewidth Broadening Mechanisms

2.5.1 Spin-relaxation

Another aspect of EPR in solids that needs to be addressed is energy flow rates. EPR spectra are heavily influenced by how excited spin states relax to lower energy states. The two most common processes for spin relaxation are spin-lattice T_1 and spin-spin T_2 mediated. The dominant mechanism for relaxation is dependent on the local environment,

for example an electron spin relaxation can be dependent on the availability of local spins or lattice vibrational modes for energy transfer. Many spin-relaxation mechanisms have been well documented and include dipolar interactions between like spins, and the motion of charged carriers in the microwave field [94].

If the electron spin relaxation time τ is very long, low microwave power is required to avoid saturation effects. In the opposite case of very small τ, lifetime broadening can make transition too broad for detection. Many spin-lattice relaxation mechanisms are inversely related to temperature and cooling down the spin system to lower temperatures is often sufficient to narrow the signal and enable detection. There have been several papers calculating T_1 and T_2 by cw-EPR by means of microwave power experiments. Alternatively, pulsed EPR measurements allow for much easier extrapolation of T_1 and T_2 but may be more experimentally difficult due to small sample requirements and thus a smaller signal/noise.

2.5.2 Hyperfine broadening

If an electron is in the vicinity of a nucleus with non-zero spin, Eq. 2.1 will be modified to account for the electron-nuclear magnetic dipole interaction

$$E = \mu_B g_e B_o m_s + A m_I m_s \tag{2.10}$$

Where m_I is the nuclear spin state and A is the electron-nuclear coupling strength. For a S = ½, I = 1/2 system, there are now 4 possible quantum states, $|m_s, m_I\rangle = |-\frac{1}{2}, \pm\frac{1}{2}\rangle$ and $|+\frac{1}{2}, \pm\frac{1}{2}\rangle$. Due to quantum transition rules, the quantum number transitions $\Delta m_I=0$

and $\Delta m_s=1$ must be obeyed, so there are now two transitions that are spaced a magnetic field approximately $A/g\mu_B$ apart [88]. Coupled with spin-relaxation or other broadening mechanisms, hyperfine coupling can cause significant EPR spectral broadening. In the case of Mg^0 in GaN, many hyperfine coupling schemes can be modeled since both Ga and N are nearly 100% $I \neq 0$. Additionally, two isotopes of Ga exist, causing two different hyperfine coupling terms *A*. For example, if the hole is localized to a single N I = 1 atom, then the number of transitions will increase from one in the case of no hyperfine to three. If the hole is localized to multiple nuclei, each coupling with slightly different A_i, then all the hyperfine transitions will be smeared into one broad signal. This is the prevailing explanation for the broad 15 mT peak-to-peak linewidth seen in Mg^0.

2.6 Details of Experimental Setup

The experimental setup of a basic continuous wave EPR system can be broken into three main steps: production of microwaves of a fixed frequency, absorption of the microwaves by the sample in a resonant cavity, and detection of photons reflected. Below is an extremely simplified description of an EPR spectrometer and is only intended to explain the key processes. For a more information, C. Poole's book *Electron Spin Resonance* goes into detail of waveguides, resonant cavity geometries, and detection analysis [95]. A general schematic for our EPR system is shown in Figure 2.4.

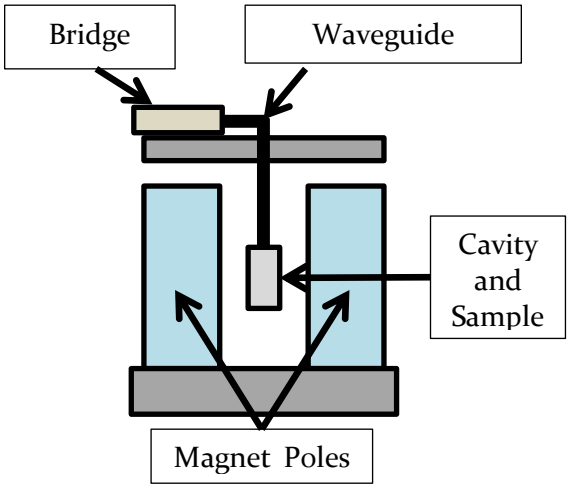

Figure 2.4. Basic EPR spectrometer schematic.

2.6.1 Before the cavity

Photons are produced in the bridge by a Gunn diode, with the frequency output determined mostly by the properties of the diode, and for EPR spectrometers typically in the 9-10 GHz range, corresponding to a wavelength of 30-33 mm. To vary the power output, the microwaves go through a variable attenuator and travel to the cavity via waveguides.

2.6.2 The cavity and resonance

The microwaves then arrive at the resonant cavity. The dimensions and shape of the cavity dictate the frequencies that resonate within the cavity. This cavity is designed specifically to maximize the magnetic field and minimize the electric field amplitude of the microwave at the location of the sample. This maximizes the EPR signal intensity. A thorough investigation of cavity designs are documented well in Poole [95]. After some minor tuning, the microwave frequency should ideally match the resonant frequency of the

cavity and the net impedance of the waveguides should match the impedance of the cavity, doing so minimizes the number of microwaves reaching the detector when not in resonance.

2.6.3 Detection

Once a spin transition occurs, i.e. when the Zeeman energy difference in spin states equals the microwave energy, resonance occurs and the sample absorbs microwaves. Specifically spins transition from m_s =-1/2 to +1/2 and change the magnetic susceptibility of the sample. This shift in cavity conductance causes a change in the number of microwaves leaving the cavity and heading to the detector; these reflected microwaves are directly related to the imaginary part of the magnetic susceptibility. The number of microwaves reaching the detector changes and produces a signal which is then recorded. Detectors are often Si-based photo-diode detectors that measure the number of microwaves reflected from the cavity. For this reason, the y-axis of a typical EPR spectrum, e.g. Figure 2.1 (b) (ii) can technically be labelled as the first derivative of the imaginary part of the magnetic susceptibility. The intensity, spacing, angular dependence, lineshape, and number of peaks in a spectrum provide information about local interactions related to the paramagnetic center.

2.7 Other Techniques

2.7.1 Raman Spectroscopy

Raman spectroscopy is a non-destructive technique used to probe low frequency modes in a system, such as rotational or vibrational motion. Based on inelastic scattering of a monochromatic light source, the change in energy will give information directly

pertaining to a specific mode of the system. In single crystals, these energy shifts will be sharp and will pertain to the vibrational modes of the crystal. Many of the vibrational modes are sensitive to the polarization of the incoming light and can be a straightforward method to identify the crystallographic orientations of a sample. More importantly, some of the vibrational modes have been directly linked to bulk crystal properties. In GaN, Raman spectroscopy has been shown to determine bulk bi-axial strain from the shift of the E_2^2 vibrational mode and relative free-carrier concentration from the A_1(LO) mode [51,52].

2.7.2 X-ray diffraction

X-rays incident on a material will scatter elastically, primarily from the electrons. The majority of scattered X-rays will cancel each other in most directions from deconstructive interference. If, however, the change in path length between scattered x-rays is equal to an integer multiple of the wavelength, then the photons will add constructively and produce a diffraction pattern, known as Bragg's Law, or

$$2d \sin\theta = n\lambda \tag{2.11}$$

where d is the separation distance between scattering centers, θ is the scattering angle, and λ is the wavelength of the X-ray. In crystals, the two scattering centers are planes, usually intersecting the centers of atoms within the lattice. The identification of a specific plane diffraction pattern is determined by its orientation, defined in Miller indices (h, k, l), and periodicity length d, which is related to the crystal lattice constants.

By knowing the bulk elemental constituents of a crystal, gallium and nitrogen for GaN, diffraction intensities from a specified (h, k, l) plane can be calculated via means of a "structure factor" S(**q**). For single crystals if the angle between the incident x-ray and/or detector changes at the same rate, a situation referred to as a θ-2θ scan, planes parallel to the surface will produce a diffraction pattern. Crystals, however, are rarely comprised of perfect repeating planes of atoms and usually contain detectable amounts of misorientation. By fixing the detector at the center of an expected Bragg reflection and tilting the sample, a process known as an omega rocking curve, the deviation of plane orientations from the ideal can be quantified. For epitaxial-grown single crystals, the lattice can become spherically curved throughout a sample, with the amount of curvature quantified by the radius of curvature r_c. By varying focused incident x-rays on different parts of the wafer, the radius of curvature can be quantified as

$$r_c = \frac{\Delta x}{\Delta \omega_{peak}} \tag{2.12}$$

where Δx is the change in sample position, and $\Delta\omega_{peak}$ is the change in the rocking curve peak position in radians.

2.8 Controversy with an Axial Localized Mg Hole

Initially, DFT computations predicted that the hole was localized on a neighboring axial nitrogen atom [82]. Experimental magnetic resonance results on heteroepitaxial thin-film samples agree with the ground state hole on an axial nitrogen neighbor, with the added requirement that the hole was delocalized partially both to neighboring basal

nitrogen atoms and to nearby molecular orbitals [81]. Variation of g-factors seen between different thin-film samples is explained by either a change in covalency factor g_l or trigonal crystal field magnitude δ . Several significant results have now added controversy to the nature of localization of the Mg acceptor. Firstly, Glaser et al. attributed a highly anisotropic signal with $g_{\parallel} = 2.19 \pm 0.01$ and $g_{\perp} \sim 0$ seen in homoepitaxial films to the Mg acceptor involved in the shallow donor – shallow acceptor PL band with zero-phonon-line at 3.27 eV and accounted for the different EPR g-factor characteristics by the relief of non-uniform strain inherent to heteroepitaxial films [83]. While the g-factor anisotropy could be effectively modeled in heteroepitaxial thin-film samples, where the magnitude of δ is expected to be large, the g-factor anisotropy observed in low strain homoepitaxial films were not able to be effectively described in a model where the hole is localized to the neighbor axial N atom. Secondly, both PL measurements and DFT calculations provide evidence that the Mg hole is well localized.

As an alternative, Aliev et al. applied a crystal field model to the hole at the Mg acceptor in GaN and demonstrated that signals seen in the heteroepitaxial and homoepitaxial films could be adequately described by a hole residing on a basal nitrogen, labelled B in Figure 1.2 (b). The model, further referred in this text as the **basal-N model**, used atomic p-orbitals that were subjected to a non-axial crystal field and $0.04 < g_l < 0.1$. Equivalently, Malyshev arrived at a similar conclusion employing localized valence band wave functions and treating the Mg hole as a shallow acceptor [96]. Both models suggest that the hole is mostly basal, rather than axial. By modeling the Mg^0 hole residing on basal sites, thin-film and free-standing GaN:Mg EPR g-factor experimental values can be well explained by a difference in the magnitude of the surrounding non-axial crystal field. It

should be noted that there is no conclusive experimental evidence that requires that the Mg^0 hole resides on a basal nitrogen site, just that the hole is on basal atomic sites.

In literature, the g-factor symmetry and anisotropy had been the only experimental evidence that supports the Mg^0 hole being localized to basal sites as opposed to an axial localization. Recently, however, the significant angular dependent EPR lineshape broadening characteristics had been effectively described by application of the basal-N model. The lineshape broadening is particularly evident in the EPR studies of free-standing crystals reported in reference 87. The observations were attributed to non-uniform bi-axial strain that was minimized in the thick free-standing crystals and maximized in thin heteroepitaxial films. Evidence for non-uniform strain in the EPR spectra implies that such strain directly affects the Mg acceptor.

My work, shown in the next chapters, addresses the disagreement around the symmetry of the Mg^0 acceptor in GaN. By performing experiments on GaN:Mg samples in a variety of crystal field environments, I show that only a basal model can correctly predict the anisotropic intensity in addition to the g-factor anisotropy. Furthermore, a non-uniform bi-axial crystal field is determined to be the dominant mechanism for the anisotropic lineshape in free-standing HVPE samples, which is consistent only in a basal model. The hole being localized to an axial nitrogen is discussed but is not effective in predicting the EPR characteristics of Mg^0 in a small bi-axial crystal field.

CHAPTER 3

EXPERIMENTAL PARAMETERS

3.1 Summary of Samples

All GaN:Mg samples used in this study were grown heteroepitaxially on sapphire substrates except for the ammonothermal-grown samples. Thin-film samples were grown by metal modulated epitaxy (MME) by Dr. A. Doolittle, metal-organic vapor phase epitaxy (MOVPE) by Dr. A.A. Allerman, hydride vapor phase epitaxy (HVPE) by Drs. J. Leach and K. Udwary, or ammonothermal by Dr. M. Bockowski. The Mg concentration in the MME sample is $1.5x10^{20}$ cm^{-3} and that in the MOVPE film is $5x10^{19}$ cm^{-3} as measured by SIMS. $Al_xGa_{1-x}N$:Mg from x = 0 to x = 0.3 MOVPE heteroepitaxy 0.5 μm thin-films with a 1.3 μm AlN buffer layer were also investigated. A collection of millimeter-thick crystals grown on sapphire by hydride vapor phase epitaxy (HVPE) was also studied with Mg concentrations varying from $4x10^{17}$-$6x10^{18}$ cm^{-3}. As the HVPE sample cooled after growth, the GaN separated from the substrate due to thermal stress and was polished, resulting in free-standing GaN doped with 3.0×10^{18} cm^{-3} Mg. GaN:Mg seed-grown ammonothermal samples were also investigated. The detailed growth process and additional characterization was described in previous sections and in other work [30,37,87,97]. Dopant concentrations, GaN:Mg sample thickness, and expected dislocation density are summarized in Table 3.1. Reported dislocation densities are determined via XRD rocking curve linewidths.

Table 3.1. A list of the samples used for this work. Impurity concentrations were determined via SIMS. *Not measured but based on growth conditions; these are the estimated values.

Growth method	Sample No.	Thickness (μm)	Mg (10^{18} cm^{-3})	Threading Dislocation density (cm^{-2})	O (10^{17} cm^{-3})
HVPE free-standing	HVPE-1	1000	1.5	$<10^7$	0.2
	HVPE-2	1000	6	$<10^7$	0.2
	HVPE-3	1000	3	$<10^7$	0.2
	HVPE-4	1000	0.4	$<10^7$	0.2
Ammonothermal free-standing	AMMO-1	430	2.1	$5x10^4$	0.88
	AMMO-2	661	7.2	$5x10^4$	2.6
	AMMO-3	567	19	$5x10^4$	15
HVPE thin-film	HVTF-1	12	10*	10^9*	0.2*
	HVTF-2	6	10*	10^9*	0.2*
MOVPE thin-film	MOVPE-1	0.47	30	10^9	0.3
	MOVPE-2	0.9	30	10^9	0.3
	MOVPE-3	0.9	30	10^9	0.3
	MOVPE-4	0.5	30	10^9	0.3
MME thin-film	MME-1	0.37	150	$<10^{10}$	0.1*
	MME-2	0.48	150	$<10^{10}$	0.1*
	MME-3	0.42	150	$<10^{10}$	0.1*
	MME-4	0.24	200	$<10^{10}$	0.1*

3.2 X-band EPR

Angular-dependent EPR measurements were performed at 3.5 K using an X-band Bruker EPR spectrometer with the static magnetic field in a plane containing the c-axis, as the schematic shows in Figure 3.1. The microwave magnetic field was oriented perpendicular to the static magnetic field. The angular-dependent zero-crossing of the Mg-related EPR signal was fit to a model with axial symmetry along the c-axis. The g-factors are determined from the standard resonance condition:

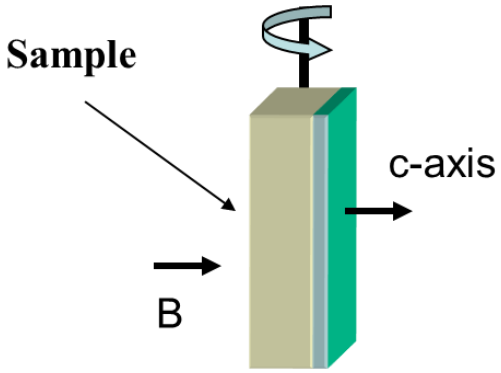

Figure 3.1. Schematic of how samples are rotated for EPR angular dependent measurements.

$$hf = \mu_B \vec{\mathbf{B}}^T \cdot \vec{\mathbf{g}} \cdot \vec{\mathbf{S}} \tag{3.1}$$

where h is the Planck constant, f is the microwave frequency, μ_B is the Bohr magneton, and $\vec{\mathbf{g}}$ is the g-factor matrix for the defect. The corresponding g-factor matrix anisotropy for Mg in GaN can be expressed with two physical parameters intrinsic to the paramagnetic defect given by the equation

$$g^2 = g_{\parallel}^2 \cos(\theta - \theta_o)^2 + g_{\perp}^2 \sin(\theta - \theta_o)^2 \tag{3.2}$$

where θ is the angle between the c-axis and the static magnetic field **B**, $g_{\parallel}$ and $g_{\perp}$ are the g-factors with the static field parallel and perpendicular to the c-axis, respectively, and θ_o accounts for initial sample misalignment. The intensity of the EPR signal was determined by numerical double integration, as described in section 2.4, and included baseline subtraction. The relative uncertainty is estimated to be 10%.

3.3 EPR Frequency Dependent Measurements

EPR frequency dependent measurements were performed at 3.0 K in the range of 37-130 GHz at the National High Magnetic Field Laboratory (NHMFL) in the laboratory of Dr. Steven Hill. Jonathan Marbey operated the equipment with experimental design and discussion from me. Microwave frequencies were generated using an ABmm Millimeter-wave Vector Network Analyzer in conjunction with a series of Shottky diodes to achieve harmonic multiplication as described by M. Mola et al. [98]. The experiment was carried out in a transmission set up to avoid any distortion of the spectral line shape that would otherwise be present in a typical cavity perturbation measurement where the sample exhibits strong dispersion. Similar to X-band EPR, a lock-in amplifier was used to increase the signal-to-noise ratio and is described in the EPR detection section 2.5.3 of this document. Phase-amplitude mixing was minimal, but nevertheless corrected for in post-processing data analysis. Transmission line-shapes were fit to a Lorentzian function and the full width at half maximum (FWHM) is reported. I also observed frequency-dependent linewidth results from absorption cavity EPR systems in other HVPE Mg-doped free-standing samples. There was significant concern that the samples from absorption-mode measurements were overloading the cavity and creating instrumentally distorted lineshapes, therefore only transmission EPR frequency-dependent measurements are shown in this work.

3.4 X-ray Diffraction

X-ray rocking curves were taken for the (002) and (006) plane at points laterally across a 14 mm length for HVPE free-standing and MOVPE thin-film samples, as shown

in Figure 3.2 to determine the radius of curvature r_c, a method applied successfully by other authors and described in section 2.6.1 [99]. For given r_c and sample dimensions, a solid angle was calculated and the resulting variance in g-factors, Δg, was determined from differentiating Eq. 2.7. Taking the derivative of the resonance equation 3.1 for magnetic field zero-crossing Δg can be related to the EPR linewidth ΔB

$$\Delta B = \frac{2h\nu}{\mu_B}\left(\frac{1}{g - \Delta g} - \frac{1}{g + \Delta g}\right) \tag{3.3}$$

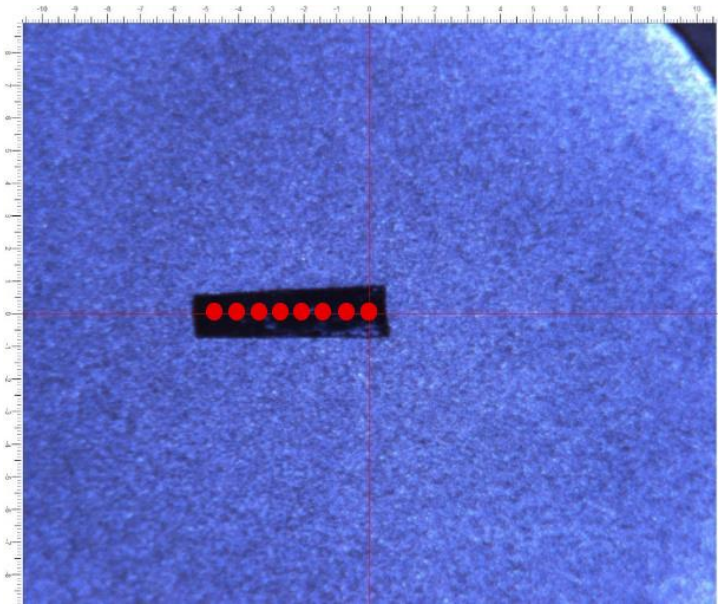

Figure 3.2. Image of HVPE sample with the c-axis pointing out of the picture. Each circle represents a point where XRD rocking curves were performed.

The distribution of Δg from crystal curvature gives rise to a frequency dependent linewidth and was compared to the experimentally observed frequency dependent linewidth.

3.5 Computational Procedure

The angle-dependence of the g-factor and spectral intensity are determined by the axial crystals field Δ_z, non-axial field Δ_x, spin-orbit coupling λ, and orbital g-factor g_l as shown in the Appendix. In the present work, we optimize Δ_x to best fit the calculated and experimental angular intensity dependent data and report the subsequent g-factor anisotropy. To calculate EPR intensities and g-factors, wavefunctions were calculated using 2p orbitals and applying the Hamiltonian used by Aliev et al. that successfully explained the Mg g-anisotropy [84]

$$H = \Delta_z\left[\hat{L}_z^2 - l(l+1)/3\right] + \Delta_x\left[\hat{L}_x^2 - l(l+1)/3\right] + \lambda \mathbf{L}\cdot\mathbf{S} \tag{3.3}$$

EPR g-factors were computed by using

$$g_x = 2\left|\langle i|\left(g_e\hat{S}_x + g_l\hat{L}_x\right)|j\rangle\right| \tag{3.4a}$$

$$g_y = 2\left|\langle i|\left(g_e\hat{S}_y + g_l\hat{L}_y\right)|j\rangle\right| \tag{3.4b}$$

$$g_z = 2\left|\langle i|\left(g_e\hat{S}_z + g_l\hat{L}_z\right)|i\rangle\right| \tag{3.4c}$$

where g_e is the free electron g-factor factor of 2.002319, g_l is the orbital reduction factor, and $|i\rangle$ and $|j\rangle$ are the degenerate ground state wavefunctions obtained from Eq. (3.3) [100]. To maintain the observed axial symmetry, $g_x \approx g_y = g_\perp$, the axial crystal field was constrained such that $|\Delta_z| \gg |\lambda|$ and $|\Delta_z| \gg |\Delta_x|$. Additionally, the sign of the axial crystal field was negative and $g_l = 0.10$ so that calculated g-factors could match the experimental

anisotropy, as explained by previous authors [84]. In the spin-orbit coupling term, λ was chosen to be -1 meV, in agreement with the factor found in homoepitaxial GaN [101]. The axial field values in the first term were -5 meV and -15 meV for the free-standing and thin-film calculations, respectively. These axial crystal field values are similar to those found from photoreflectance spectroscopy reports in GaN thin-films[102]. A potential explanation for the small orbital reduction factor g_l and spin-orbit coupling term λ is electron-phonon coupling in the form of a dynamic Jahn-Teller effect, as suggested by previous authors and discussed further in section 4.8 [96,103].

The EPR intensity was calculated by

$$I \propto |\langle i''|H_{mw}|j''\rangle|^2 \left(\frac{d(E_i - E_j)}{dB}\right)^{-1} \tag{3.5}$$

where the first term is the transition matrix element due to the perturbing microwave field and the second term is the frequency-to-field conversion factor which is proportional to 1/g [104,105]. The dipole moment operator associated with the microwaves incident on the sample is $H_{mw} = \mu_B B_1 g_\perp \hat{S}_\perp$, where B_1 is the amplitude of the microwave magnetic field. First order corrections to the ground states $|i\rangle$ and $|j\rangle$ used previously were calculated and are reported here as $|i''\rangle$ and $|j''\rangle$. Second and third order correction terms were inspected but were too small to affect the results. Full computational characterization of the Mg acceptor EPR properties are summarized in the appendix.

3.6 Data Fitting

For much of the analysis in this work, data are fit to closed form functions with k parameters $f(x;a_k)$ and the parameters of those functions are interpreted. The best fit to a function is determined by varying the function's parameters a_k and finding the minimum value of chi-square χ^2 which is defined as

$$\chi^2 = \sum_{i=1}^{N} \frac{\left(O_i - f_i(a_1, a_2, \ldots.)\right)^2}{\sigma_i^2} \tag{3.6}$$

where O_i is the observed (experimental) data point, f_i is the calculated data point, with variance σ_i for a given data point from a set of N data points. For example, in this work the g-factor anisotropy was fit by using Eq. 2.9 as the function and the parameters $g_{\parallel}$ and $g_{\perp}$ were determined by minimizing Eq. 3.6. The simplex method was applied via the OriginPro 8 to vary the parameters a_k and find the minimum χ^2 for a given dataset and function. In all simplex fitting, the maximum number of iterations was set to 400 with a relative tolerance of $1x10^{-9}$.

When optimizing Hamiltonian parameters to extract crystal field values, no closed-form expression exists for the calculated angular dependent g-factor or EPR intensity and the simplex method cannot be applied. Additionally, when fitting a singular EPR lineshape to multiple peak functions, the number of variables and parameter space is too great and the simplex method fails to return good fits. In this case, a modified genetic

algorithm similar to the method discussed in Y.J. Cao et al. was applied to vary parameters and minimize χ^2 [106].

CHAPTER 4

RESULTS AND DISCUSSION

Reported below are the findings of Mg-doped GaN samples from EPR experiments. The best fit $g_{\perp}$ and $g_{\parallel}$, impurity concentrations, and GaN:Mg thickness are reported for all samples used in the study shown in Table 4.1. By varying the bi-axial crystal field magnitude in a crystal field model, we are able to predict the g-factor anisotropy in a wide variety of strain environments (section 4.2) [84,96]. In further development of the crystal field model, it is shown that the change in crystal field magnitude alters the EPR anisotropic intensity (section 4.3). Finally, the presence of a non-uniform field throughout a sample is demonstrated to produce an anisotropic linewidth (section 4.6). Other frequency-dependent linewidth broadening mechanisms were investigated and shown to not contribute significantly to the experimentally observed broadening (section 4.7). Finally, the EPR temperature dependence is shown in section 4.8 with some conjecture about the mechanisms of broadening.

4.1 EPR g-factors

4.1.1 Thin-film samples

The 9.4 GHz EPR angular dependence of the g-factor seen in the μm-thick heteroepitaxial thin-films and mm-thick free-standing GaN:Mg samples are similar to those reported by others and is identified as being related to the neutral Mg acceptor. The measured SIMS Mg concentration, GaN:Mg sample thickness, and fit $g_{\perp}$ and $g_{\parallel}$ are

summarized in Table 4.1. An example resonant magnetic field B_o at two different crystal orientations for a MOVPE sample is shown by red dots in Figure 4.1 (a). The EPR Mg^0 signal is well described as a S = 1/2 spin center with a peak-to-peak linewidth of 15 mT. By applying the EPR resonance condition Equation 2.2 the EPR g-factor values can be calculated for a given defect. The EPR g-factor angular dependence for typical thin-film MME (black squares), MOVPE (red circles), and HVPE thin-film (blue triangles) samples are shown in Figure 4.1 (b). The solid lines represent best fits of Eq. 3.2. Thin-film MOVPE g-factors were determined to be $g_{\|}$ = 2.08 and $g_{\perp}$ = 1.99 and those of the MME sample, $g_{||} = 2.06$ and $g_{\perp} = 2.01$, similar to results found in the literature [83,107]. The HVPE thin-film could not be measured in the range 60-120^o due to an increasing background interference from the signal and therefore the fit $g_{\perp}$ is not as precisely known. The anisotropic background is predicted to originate from a conducting layer at the substrate-film interface, discussed in several papers [108,109].

Table 4.1. Growth method, SIMS Mg concentration, and fit EPR g-factor parameters for samples used in this study. *Not measured, but based on growth conditions; these are the estimated values.

Growth method	Sample No.	Thickness (μm)	Mg (10^{18} cm^{-3})	$g_{\parallel}$	$g_{\perp}$
HVPE free-standing	HVPE-1	440	1.5	2.22(1)	0.26(5)
	HVPE-2	800	6	2.21(1)	0.42(6)
	HVPE-3	1000	3	2.183(7)	0.28(4)
	HVPE-4	1000	0.4	2.182(6)	0.18(7)
Ammonothermal free-standing	AMMO-1	430	2.1	2.110	2.000
	AMMO-2	661	7.2	2.094(5)	1.965(7)
	AMMO-3	567	19	2.067	2.009
HVPE thin-film	HVTF-1	12	10*	2.116(5)	1.93(2)
	HVTF-2	6	10*	2.109(7)	1.93(1)
MOVPE thin-film	MOVPE-1	0.47	30	2.077(1)	1.999(1)
	MOVPE-2	0.9	30	2.087(1)	1.999(1)
	MOVPE-3	0.9	30	2.094(3)	1.995(2)
	MOVPE-4	0.5	30	2.088(2)	1.991(1)
MME thin-film	MME-1	0.37	150	2.0616(5)	2.0147(6)
	MME-2	0.48	150	2.0472(2)	2.0180(2)
	MME-3	0.42	150	2.04	2.03
	MME-4	0.24	200	2.02	2.03

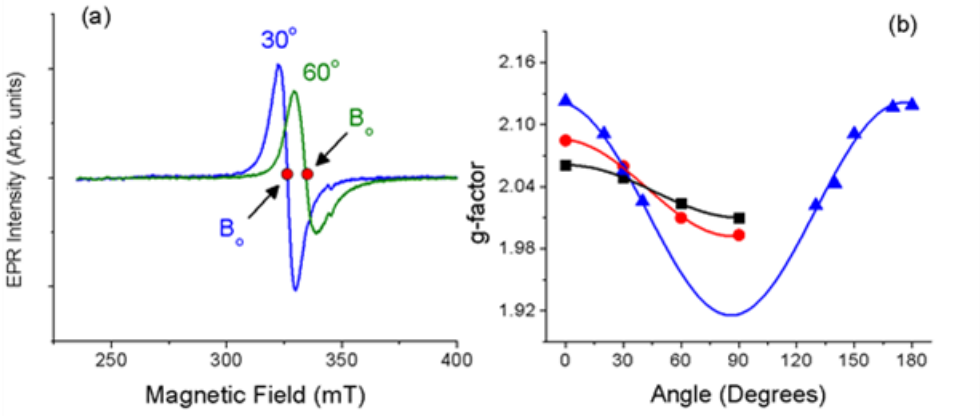

Figure 4.1. Example spectra of the Mg-related EPR signal obtained at 9.4 GHz and 3.5 K observed in a MOVPE thin-film with the angle between the c-axis and static magnetic field oriented at 30° (blue) and 60° (green). The zero-crossing B_o for each angle is highlighted at the red circle. (b) EPR g-factor angular dependence for thin-film MME (black squares), MOVPE (red circles), and HVPE thin-films (blue triangles) samples. Lines are best fits of Eq. 3.2 to the data.

4.1.2 Free-standing samples

In this work, two different types of free-standing samples were investigated: heteroepitaxial grown HVPE and seed-grown ammonothermal. The spectroscopic characteristics of the Mg-related EPR signal in free-standing HVPE samples differ significantly compared to thin-films. Firstly, the lineshape and linewidth is more angular dependent and the lineshape asymmetry is reversed compared to thin-films, where at angles higher than 20^o the high field peak has a smaller linewidth and is more intense than the low field peak, as seen in Figure 4.2 (a) for 60^o. The peak-to-peak linewidth is seen to monotonically increase as θ increases but is difficult to quantify since the Mg signal cannot adequately be described by a single Lorentzian lineshape at angles higher than 20^o. Secondly, the observed g-factor anisotropy is much more dramatic as shown in Figure 4.2 (b) with optimally fit values of $g_{\parallel} = 2.18$ and $g_{\perp} = 0.28$ for Sample 1 (AB3589). Due to the large anisotropy, only angles up to 70^o could be measured before the resonance occurred at B larger than the 1 T magnet limit as denoted by the dotted horizontal line in Figure 4.2 (b). The observed g-factor and lineshape anisotropy in free-standing HVPE samples agrees well with values reported in homoepitaxial thin-films GaN:Mg from other authors [37,83].

In contrast, the ammonothermal GaN:Mg samples, which are grown homoepitaxially via seed growth, has anisotropic characteristics more similar to heteroepitaxial HVPE or MOVPE thin-film samples.

In this dissertation, I will show that the differing behavior of the two free-standing samples are consistent with the crystal field model and can be used as a tool to probe the bi-axial strain local to the Mg acceptor (section 4.2).

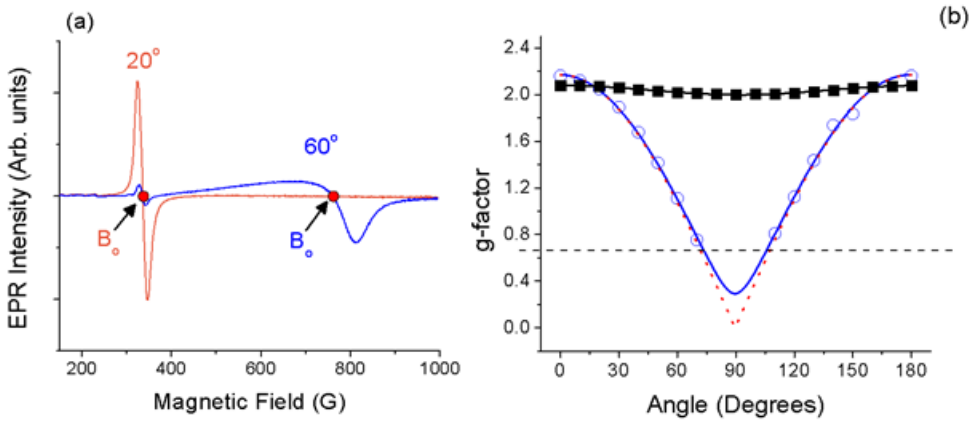

Figure 4.2. (a) Example spectra of the Mg-related EPR signal obtained at 9.4 GHz and 3.5 K observed in a HVPE free-standing sample oriented at 20° (orange) and 60° (blue). The zero-crossing B° for each angle is highlighted as the red circle. (b) EPR g-factor angular dependence HVPE free-standing samples (blue circles). The thin-film MOVPE data (black squares) is shown for reference. Lines are best fits of Eq. 3.2 to data. The dotted red line is the g-factor angular dependence extracted from fitting the intensity angular dependence. The horizontal dashed black line indicates the minimum g-factor accessible with the 1 T magnet at 9.4 GHz.

4.1.3 Reduction of g-factor anisotropy

EPR g-factor values are sensitive to changes in the defect's local environment. Depending on the local perturbation, the g-factor of a defect can change in magnitude and/or angular dependence. In heteroepitaxial thin-film $Al_xGa_{1-x}N$:Mg, the Mg^0 EPR signal becomes less anisotropic in g-factor and lineshape as x increases, as shown in Figure 4.3 (a). The g-factor anisotropy is seen to decrease as Al content increases from x = 0 to x = 0.28, with $g_{\|}$ reduced from 2.09 at x = 0 to 2.01 at x = 0.28 and $g_{\perp}$ changing less than 0.02 over the Al alloying range as shown in Figure 4.3 (b) [110]. In free-standing samples, it was observed that the measured SIMS concentration of Mg affects the Mg^0 g-factor as seen in Figure 4.4, where increasing Mg concentration increases $g_{\perp}$ but $g_{\|}$ remains the same. To more clearly show the changes in

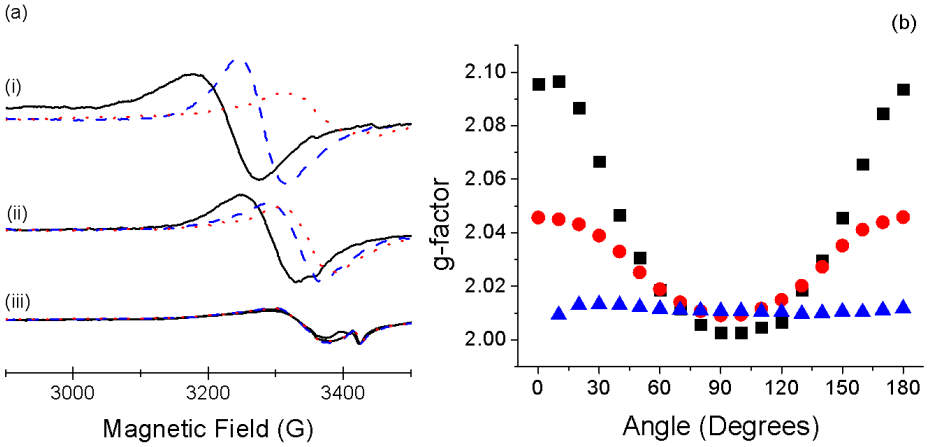

Figure 4.3. (a) 3.5 K Mg-related EPR spectra of RTA $Al_xGa_{1-x}N$ with the magnetic field oriented at 0° (solid black), 30° (dashed blue), and 90° (dotted red) to the c-axis for (i) x = 0, (ii) x = 0.08, and (iii) x = 0.28. (b) g-factors obtained from RTA $Al_xGa_{1-x}N$ for x = 0 (black squares), x = 0.08 (red circles), and x = 0.28 (blue triangles).

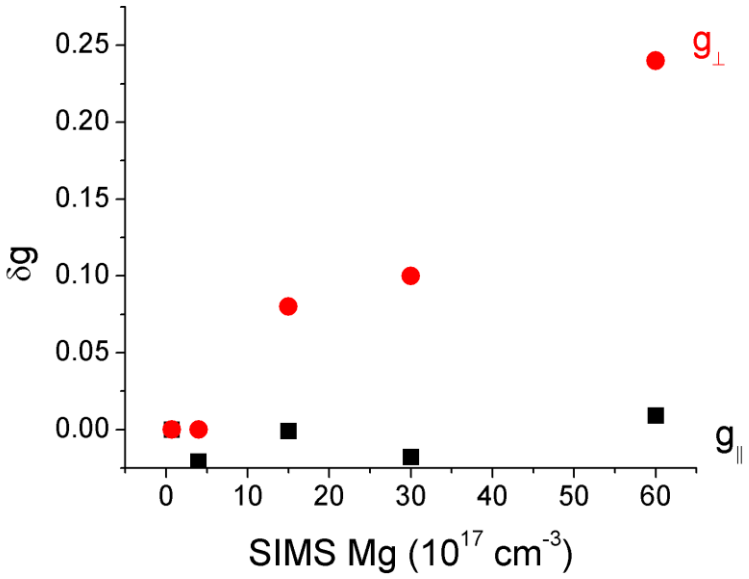

Figure 4.4. Change in g-factor values fit from Eq. 3.2 as a function of measured Mg SIMS concentration for $g_{\|}$ (black squares) and $g_{\perp}$ (red circles). To make both $g_{\|}$ and $g_{\perp}$ fit in the same scale, they are subtracted from the first data point at SIMS Mg concentration $7x10^{16}$ cm^{-3}, i.e. $\delta g = g(x) - g(7x10^{16}\ cm^{-3})$ where x is the Mg concentration.

g, the g-factors are subtracted by the g-factor for the sample with the lowest Mg concentration. The SIMS Mg concentration has been observed to change the Mg-related EPR g-factor in thin-films, so seeing a similar phenomenon in free-standing samples is not surprising [111].

The decreasing g-factor anisotropy of Mg^0 in both the thin-film and free-standing case suggests a change in local crystal fields surrounding the defect. When Al replaces a Ga atom in the crystal lattice, local strain around the Mg^0 will increase. If enough Al is added to a sample, as is the case for these samples, the local changes in atomic spacing will affect bulk properties such as lattice spacing and can be seen via XRD [112]. By increasing the Al content in GaN:Mg, local strain around Mg acceptors will increase, therefore changing the local environment and resulting EPR g-factor. Similar arguments cannot be made for increasing the Mg concentration in GaN, where 1 Mg replaces 1 in 10^5 Ga atoms. As seen by C.G. Van de Walle et al., the strain field produced by a Mg_{Ga} impurity is quite localized and requires a significant amount of Mg incorporation for an observable effect with the crystal lattice parameter changing $\Delta a/a \approx 10^{-6}$ at Mg concentrations of 10^{18} cm^{-3} [113]. Therefore, I suggest that a secondary effect, related to increasing the Mg concentration, plays a role in affecting Mg^0 centers as discussed at the end of section 4.2.

4.2 Evidence of Bi-axial Crystal Field Effects From the g-factor

A crystal field model that uses the Hamiltonian in Eq. 3.3 can be used to effectively predict the strikingly different characteristics of the EPR Mg^0 signal observed in free-standing and heteroepitaxial thin-film samples. First, focus will be put on modeling the g-factor anisotropy, which is significantly different between thin-film and free-standing

samples. A more detailed explanation can be found by Aliev et al., but an abridged version is summarized as follows [84]. Starting with 2p orbitals as the basis set, the axial crystal field splitting Δ_z is chosen to be negative so that the lowest energy wavefunctions are then p_x and p_y. Next, a bi-axial crystal field, Δ_x, is introduced, the sign of which is not important. Also, the orbital angular momentum is significantly quenched, i.e. $g_l < 1$. By varying the magnitude of Δ_x, the g-factor principle values, $g_\perp$ is seen to change dramatically as is plotted in Figure 4.5. The Mg-related EPR signal can now be modeled in all samples by varying the magnitude of Δ_x, further supporting the basal-N model. If Δ_z is positive, then p_z will be the lowest energy wavefunction and calculated g-factors will have the opposite angular dependence ($g_\parallel < g_\perp$) which is not seen experimentally for Mg^0. Alves et al. have proposed forcing the wavefunction to be averaged out to all wavefunctions p_x ,p_y, and p_z and varying the orbital reduction factor g_l (labelled as a covalency factor *k* in their work), but only thin-film samples are able to be effectively modelled [81].

The basal-N model described above is supported by all the GaN:Mg samples described in Table 4.1. The samples can be sorted into three different regions in Figure 4.5 that are distinguished by the magnitude of Δ_x. The samples with the largest bi-axial crystal field, and therefore smallest g-factor anisotropy, are MME samples which are less than 0.4 μm thick on a latticed-mismatched non-native substrate, have the highest concentration of Mg ($1.5x10^{20}$ cm^{-3}), and highest density of dislocations ($>10^{10}$ cm^{-2}) of all GaN:Mg samples; all of these properties lead to large strain fields around the Mg acceptor and, therefore, large crystal fields and isotropic g-factors; these samples are sorted into region A in Figure 4.5. In MOVPE and HVPE heteroepitaxial thin-films mechanical strain is reduced by several factors - such as increased thickness of the GaN:Mg layer, reduced

concentration of Mg, and reduced density of dislocations. These samples are sorted into region B. The reduction in both the Mg concentration and of physical strain sources decreases the magnitude of the bi-axial crystal field, and thus increases g-factor anisotropy.

The ammonothermal samples are measured to have very low bulk crystal strain and a small threading dislocation density, as evidenced by XRD measurements [114]. However, the g-factor anisotropy is similar to that seen in heteroepitaxial thin-film samples $g_{\parallel} - g_{\perp} \approx 0.1$, which suggests a large bi-axial crystal field. Usually, the source of the non-axial crystal field has, quite naturally, been attributed to originate from physical, or mechanical, strain mechanisms because Δ_x is largest in the thinnest films where dislocations are the maximum. In mechanically strained systems, it is the local change in lattice parameters that induces an additional crystal field due to the breaking of the bulk symmetry. However, dislocations need not be the sole contribution to a non-axial crystal field with a large magnitude and is demonstrated by the ammonothermal samples.

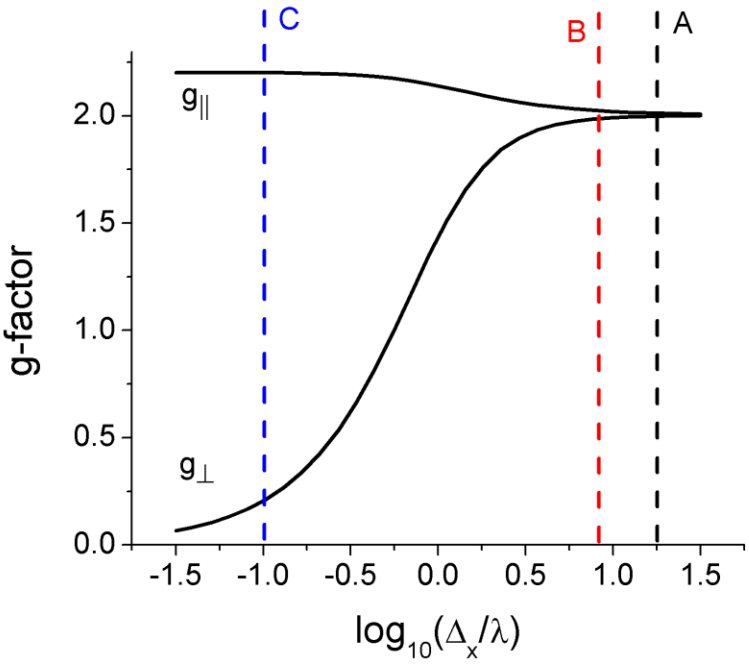

Figure 4.5. The g-factors for holes localized to acceptor sites as a function of a varying bi-axial crystal field in the x-direction. The axial crystal field, spin-orbit coupling, and orbital reduction factor is fixed at Δ_z = -15 meV, λ = -1 meV, and g_l = 0.1.

In ammonothermal GaN, Oxygen replaces nitrogen sites in GaN and is a shallow donor with an ionization energy of ~34 meV [46]. The 10^{18} cm^{-3} oxygen leads to a distance between randomly spaced O donors and Mg acceptors atoms of less than 10 nm. If the samples are p-type then, assuming complete compensation, all the O sites will be ionized and create a large crystal field, originating from the charge distribution within the bulk sample. Therefore, one would expect EPR characteristics similar to those seen in heteroepitaxially thin-films if the concentration of compensated O were high enough. Homoeptiaxially grown ammonothermal p-type GaN doped with $7.2x10^{18}$ cm^{-3} Mg and $2.6x10^{17}$ cm^{-3} O, were measured at 3.5 K and 10 GHz in the same manner as the samples discussed above. The results reveal a nearly isotropic EPR g-factor and intensity, even though the dislocation density is lower than HVPE free-standing samples ($<10^7$ cm^{-2}). The

isotropic signal in the ammonothermal samples demonstrates the universal applicability of the crystal field model with bi-axial strain.

Finally, HVPE free-standing samples have a reduced dislocation density and Mg concentration, both of which reduce the magnitude of physical strain and the resulting crystal field compared to the other samples discussed above. The large g-factor anisotropy assigns HVPE free-standing samples to region C in Figure 4.5.

These assignments in local bi-axial crystal field strength are consistent with bulk GaN Raman spectroscopy measurements, where the magnitude of the frequency shift in the E_2 vibrational mode is a marker for bulk bi-axial strain. Raman measurements carried out by Dr. William Willoughby and Kathryn Ham showed that MME thin-film samples have the largest E_2 shift of 571.5 cm^{-1}, indicating a large bi-axial strain. Thin-film MOVPE samples, which are expected have less bi-axial strain had a E_2 shift of 570.5 cm^{-1}. and free-standing HVPE samples, which should have minimal bi-axial strain, 569.5 cm^{-1}, as shown in Figure 4.6. This provides evidence that the in-plane strain for bulk GaN is highest in thin-film samples, and relaxes in free-standing GaN, consistent with reports by other authors [85,115]. However, Raman spectroscopy is unable to determine strain local to defect sites, and has additional difficulty separating hydrostatic and bi-axial strain.

The decreased anisotropy in $Al_xGa_{1-x}N$ samples can now be understood via the changes in the magnitude of the bi-axial crystal fields. As x increases, local strain distortions from Al atoms will cause an increased magnitude of crystal field, some of which will have a bi-axial component, thus reducing the observed g-factor anisotropy. However, the same analysis on decreased g-factor anisotropy with increasing Mg concentration is not consistent with DFT computational results as the local strain distortions were calculated to

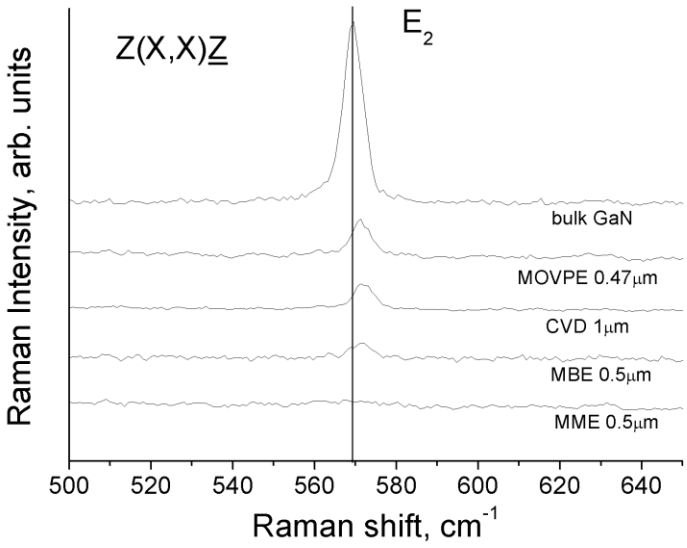

Figure 4.6. Room temperature Raman spectra using a 535 nm light source of GaN:Mg samples grown various ways.

change the bulk lattice parameter by less than 0.001% for Mg concentrations of 10^{18} cm^{-3} [113]. However, transmission electron microscopy experiments show that the density of stacking faults increase with increasing Mg concentration in GaN [44]. Energy dispersive x-ray analysis also reveals that the Mg atom is 3-5 nm from the stacking fault plane, which can impart local mechanical strain to the Mg acceptor.

4.3 Evidence of Bi-axial field from Intensity Angular Dependence

In addition to the g-value angular dependence of a paramagnetic center, the EPR signal intensity can provide identification and, as will be shown for the case of GaN:Mg, characterization of the local environment. The intensity of an EPR transition is directly proportional to the number of paramagnetic centers. The intensity of any given EPR transition can be expressed as

$$I \propto |\langle i|\boldsymbol{H}_{mw}|f\rangle|^2 \cdot \left(\frac{d(E_a - E_b)}{dB}\right)^{-1} \cdot (p_i - p_f) \tag{4.1}$$

The first term is the transition probability with a perturbing microwave field $H_{mw}=\mu_B B_1 g_\perp \hat{S}_\perp$ where B_1 is the magnetic field strength of the microwave incident on the sample. The $|i\rangle$ and $|f\rangle$ states are the quantum states before and after the spin flip transition, respectively, assuming little to no mixing from the static magnetic field. For thin-film samples, this will be shown to be a valid simplification.

The second term in Eq. 4.1 is a frequency-to-field conversion factor that was discovered in 1975, quite late in EPR history [104]. This term, to first order, is proportional to 1/g and is significantly important in calculating angular dependent intensities in systems with a large g-factor anisotropy. J.R. Pilbrow has written a very thorough expansion of the "Aasa and Vanngard 1/g factor", including the more complicated S > 1/2 case [105]. Nehrkorn et al. has a more general discussion on the topic of magnetic dipole transitions in EPR [116]. Finally, the third term accounts for the population difference between the initial p_i and final state p_f

The same crystal field model used to explain the g-anisotropy should also be able to predict the intensity of the EPR spectra. That is, in addition to the bi-axial crystal field Δ_x playing a dominant role in g-factor anisotropy, it has been predicted that the magnitude of both axial and basal crystal fields can significantly change the angular dependent intensity [117]. Here we provide experimental evidence of this claim. The filled squares in Figure 4.7 (a) illustrate the angular dependence of the intensity for the free-standing sample. We first consider a model using only an axial crystal field (i.e. $\Delta_x = 0$), a method

previously used to model shallow acceptors by Patel et al. [117]. The calculated EPR intensity is plotted as the dotted blue line in Figure 4.6 (a). The predicted EPR intensity should be proportional to $\tan^4(\theta)$ only when $(g_\perp/g_\parallel)\tan\theta \ll 1$ where $g_\perp$ and $g_\parallel$ are the experimentally determined g-factors obtained from Eq. 3.1. Thus, one would expect the calculation to agree with the data well at small angles and begin to deviate at the larger angles. In fact, the opposite is seen and there is increased agreement at higher angles. However, with the addition of a small non-zero non-axial crystal field term expected for free-standing thick crystals ($\Delta_x = 10^{-5}$ meV) the calculated angular dependent intensity becomes non-zero at 0^o and matches well with experimental data at 0-60^o and 120-180^o. We note that although the optimal Δ_x is small, the value must be non-zero and positive to fit the low angle data for free-standing samples as seen by the solid black line shown in Figure 4.7 (a). We acknowledge, however, that the small size of Δ_x suggests different

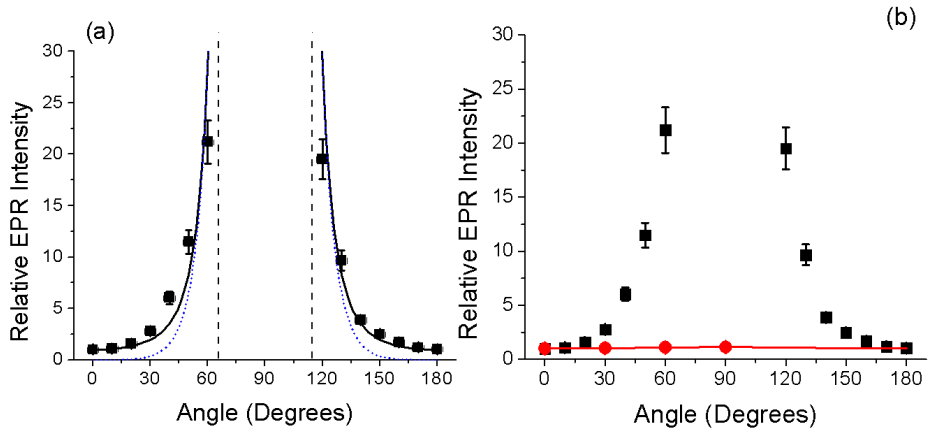

Figure 4.7. EPR Intensity angular dependence of (a) free-standing (black squares) and (b) both free-standing (black squares) and thin-film MOVPE (red circles) samples at 9.4 GHz. Solid lines are simulations of EPR intensity using the Hamiltonian in Eq. 3.3. The dotted blue line in (a) is a fit using the same equation but with Δ_x=0. Vertical dashed black lines indicate inaccessible angles due to the signal's highly anisotropic g-factor.

factors may control the non-zero intensity. For instance, the addition of nitrogen 2s orbitals to the pure p-orbitals used here might have enough of an effect at parallel orientation as to induce a detectable EPR intensity without significantly altering the dramatic affects seen at perpendicular orientation, which is the focus of the model.

After finding the crystal field parameter that optimally fits the free-standing anisotropic intensity, g-factors are then computed using Eq. 3.4. The resulting g-factor calculations agree with the experimentally determined $g_{\parallel}$, but deviate significantly from $g_{\perp}$. To investigate the source of this discrepancy, the angular dependence of the g-factor calculated from the intensity was compared with that determined by fitting Eq. 3.1 to the experimentally measured $g(\theta)$. Figure 4.2 (b) shows the results, where the g-factors obtained from fitting the anisotropic intensity are represented by the dotted red line and those obtained from Eq. 3.1 are shown as the solid blue line. The comparison indicates that a discrepancy occurs only at angles near 90^{o}, where spectra are not able to be measured. The differences between the $g_{\perp}$ calculated from Eq. 3.1 and extracted from the intensity are therefore within the uncertainty of the $g(\theta)$ measurement.

The angular dependence of the intensity seen in the thin-films is minimal compared to that seen in the free-standing crystals and, therefore, limited information may be extracted. A comparison is shown in Figure 4.7 (b), where filled black squares represent the free-standing GaN and unfilled red circles the thin-films. The intensity of thin-film MOVPE samples varied less than 10% between 0^{o} and 90^{o} and could be simulated (red line) only with large axial and basal crystal fields. Consistent with the g anisotropy exhibited by the MOVPE and MME samples mentioned above, the intensity of the MME samples varied no more than 5% between 0^{o} and 90^{o} and the intensity calculations predict

a larger crystal field. The smaller angle-dependent intensity, in addition to the decreased g-factor anisotropy, indicates that a larger crystal field exists in the MME samples compared to MOVPE. Using the same crystal field values as in the calculation of the angular dependent spectral intensity, a nearly isotropic g-factor was calculated and compared favorably with experimental results for both MOVPE and MME samples.

The dominant mechanism for the EPR intensity angular dependence is markedly different between free-standing samples and heteroepitaxial thin-films. The EPR intensity of a transition is determined by Eq. 3.5 and has three distinct components: the transition dipole matrix overlap $\left|\langle i|\widehat{H}_{mw}|j\rangle\right|^2$, the Aasa-Vanngard 1/g factor, and the thermal population difference. The calculated contributions from each component in Eq. 3.5 are plotted in Figure 4.8 for (a) free-standing HVPE and (b) heteroepitaxial thin-films. For angular dependent measurements, the thermal population difference is constant and is not plotted. The intensity anisotropy observed in free-standing samples are seen to be dominated by the transition dipole matrix with a minor contribution from the 1/g factor. Comparatively, the intensity from heteroepitaxial thin-films is mainly due to the 1/g factor and the transition dipole term is nearly isotropic. The reason for this is because the dipole transition matrix is approximately inversely dependent on the crystal field terms to fourth order [117].

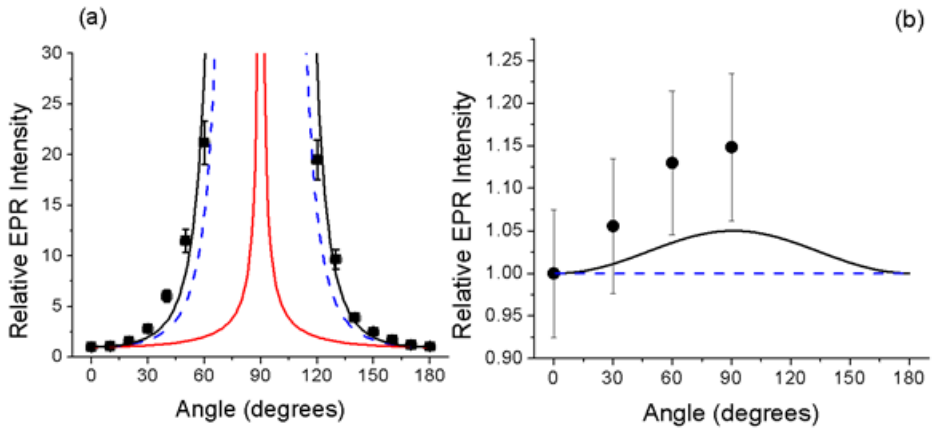

Figure 4.8. The transition probability matrix (dotted blue) and Aasa-Vanngard 1/g factor (solid red) contributions to the relative EPR intensity plotted along the product of the two (solid black) contributions to the calculated angular dependent intensity for a (a) free-standing HVPE and (b) heteroepitaxial MOVPE thin-film sample.

In the analysis of $g(\theta)$ performed by Aliev et al., a negative axial field was invoked to reproduce the observed relative values of $g_{\parallel}$ and $g_{\perp}$ ($g_{\parallel} > g_{\perp}$) [84]. The negative Δ_z leads directly to the prediction that the hole resides on a basal, rather than axial, nitrogen. To verify the necessity of a negative axial field, intensity calculations were performed assuming a positive axial field, resulting in a ground state axial hole. Although the results for the thin-films samples are non-conclusive due to the weak angular dependent intensity, the calculations for the free-standing samples not only predict that $g_{\parallel} < g_{\perp}$, as shown by previous authors, but that the EPR intensity decreases as the angle approaches 90°, inconsistent with the results shown in Figure 4.7 (a) [81,84].

4.4 Realism of Hamiltonian Parameters

There are many mechanisms that can induce additional crystal fields to the Mg acceptor in materials and, therefore, change the observed g-factor that is seen in GaN:Mg samples. Mechanical strain compresses or expands the lattice constants that, in turn, affect

the charge distribution surrounding the EPR-active defect. Independent of any defects, a non-zero axial crystal field Δ_z will be present in GaN due to symmetry breaking arguments [40,41]. Measurements of the bulk axial crystal field and band spin-orbit coupling parameters have been performed by others on UID thin-film GaN via photo-reflectance spectroscopy and obtained values of $|\Delta_z|$ =9.2 meV and λ = 18.9 meV [102]. The spin-orbit coupling parameter for point defects, however, may be effectively reduced by an increase in molecular orbital coupling, i.e. covalency, as is discussed in section 4.8. An effective spin-orbit coupling constant of -0.86 meV has been reported for uid GaN via Zeeman spectroscopy [101].

Determining the bi-axial crystal field has, however, proven to be a more arduous task. Raman experiments have shown sensitivity to crystal strain in the c-plane and that the E_2 vibrational mode shifts depending on the magnitude of strain present in the bulk crystal [32]. It has been shown, however, that hydrostatic strain and bi-axial strain each shift the E_2 mode by different amounts and separation of each component requires an analysis of the strain tensor elements, typically via XRD [118,119]. From this type of analysis, the net strain energy is calculated from the Raman E_2 shift and is shown in Table 4.2 [52,118]. To compare these numbers to those calculated for the Mg acceptor, one can use the relationship between the bi-axial strain and the energy shift in exciton luminescence established by Davydov et al. [118]. The results, shown in column 4 of Table 4.2, are of similar magnitude to the proposed meV range bi-axial crystal field for the Mg acceptor [118], and thus confirm that the values from the crystal field model are realistic.

Table 4.2. Raman shifts and calculated strain energies and their corresponding bi-axial bound exciton energy shift.

Sample	Raman E_2 shift (cm^{-1})	Strain energy (GPa)	Bound Exciton energy shift (meV)
HVPE free-standing	569.5	0.4-0.7	14
MOVPE	570.5	0.7-1.1	22
MME	571.5	1-1.4	28

4.5 Lineshapes and Linewidths

The structure of a defect's local environment has been shown to impact both the EPR anisotropic g-factor and intensity in sections 4.1 and 4.3, but the lineshape characteristics can provide additional information. In this section I will discuss the mechanism for the anisotropic EPR lineshape observed at 9.5 GHz that was proposed by Zvanut et al. [87]. In this section, I make experimental predictions based on the crystal field model from section 4.2 and provide motivation for frequency-dependent EPR measurements.

As the angle increases from 0^o to 90^o, the linewidth and lineshape of MOVPE and HVPE thin-films are observed to noticeably change as seen in Figures 4.1 (a) and 4.2 (a) respectively. At low angles, the signal is well described by a single Lorentzian line-shape, but, as θ increases, the lineshape becomes increasingly asymmetric with the low field peak having a higher amplitude and smaller linewidth compared to the high field peak. The Mg-related EPR lineshape from MME samples is isotropic with a peak-to-peak linewidth of 10 mT. An explanation and understanding of the linewidth phenomena are addressed in section 4.7.2.

It was proposed by Zvanut et al. that the bi-axial crystal field was non-uniform throughout samples, i.e. a distribution of Δ_x that results in a distribution of g-factors to model the anisotropic lineshape in GaN:Mg samples [87]. The lineshapes of both heteroepitaxial thin-film and free-standing samples can be successfully described by fitting each signal to a sum of 5 Lorentzian lineshapes of equal linewidth but varying g-factors and intensities. The variation in $g_{\|}$ between all Lorentzian lines, defined as $\Delta g_{\|}$, is small, but the variation in $g_{\perp}$, defined as $\Delta g_{\perp}$, is significant to successfully describe the anisotropic lineshape.

Table 4.3. The range of g-factors required to fit the EPR angular-dependent lineshape at 3.5 K and 10 GHz.

Sample	$\Delta g_{\|}$	$\Delta g_{\perp}$
Free-standing HVPE	0.08	0.22
Heteroepitaxy MOVPE	0.06	0.07

From Figure 4.5, varying Δ_x in regions A, B, or C will have significantly different effects in resulting EPR lineshape characteristics. In region A, both $g_{\|}$ and $g_{\perp}$ are predicted to be insensitive to a distribution of Δ_x, thus Δg will be small (<0.01) and the lineshape and linewidth of Mg^0 should be isotropic – as is confirmed in MME samples by the fact that a single Lorentzian lineshape represents the spectra well. As Δ_x decreases, small variations of Δ_x will cause larger variations in $g_{\perp}$, but leave a relatively small distribution of $g_{\|}$. In region B, an inhomogeneous Δ_x will result in a variation of $g_{\perp}$, which will cause some distortion of the lineshape and linewidth as the sample is rotated from 0^o to 90^o – an observation frequently noted by others in MOVPE GaN:Mg [83,87]. Finally, in region C, perturbations in Δ_x should result in large variations of $g_{\perp}$ and a smaller distribution of $g_{\|}$ –

consistent with the results found in Table 4.3. Therefore, the small $\Delta g_{\parallel}$ and larger $\Delta g_{\perp}$ found from lineshape modeling are consistent with crystal field model predictions.

EPR linewidth broadening due to a distribution of centers with varying g-factors, known as **g-strain**, is effective at predicting the lineshape change in both thin-film and free-standing samples. For g-strained EPR spectra, it is the magnitude of the variation of the g-factor Δg that will then dominate the linewidth. When g-factors of different centers do not vary significantly, their magnetic resonances B_o at a specified frequency can overlap and the lineshapes will be unresolved. If the g-strained lineshape is comprised of a few discrete g-factors, then performing EPR at higher microwave frequencies will increase B_o between centers with different g-factors and each individual center can be resolved, as shown in Figure 4.9 (b). However, if a continuous distribution of varying g-factors is the dominant contribution to the lineshape of an EPR transition, increasing the microwave frequency will not resolve additional structure, but instead lead to a linear increase in linewidth, the magnitude of which is dependent on Δg, furthermore Δg will vary with θ, the angle between **B** and the c-axis.

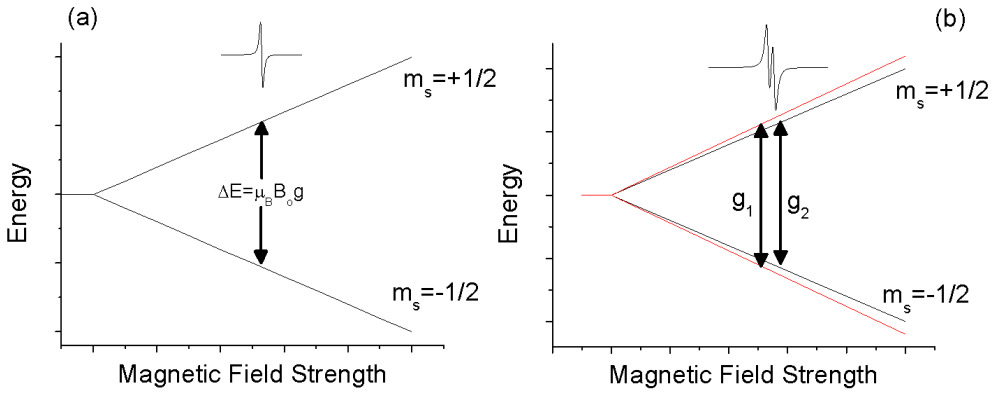

Figure 4.9. (a) A standard Zeeman energy diagram of one isolated spin S = ½ system and the resulting EPR spectrum. (b) A Zeeman energy diagram for two independent spin S=1/2 systems with slightly different g-factors and the resulting EPR spectrum.

4.6 Evidence of Crystal Field Non-uniformity

In section 4.5, non-uniformity of the crystal field was deduced from an analysis of the angular dependent line shape. The study assumed that a non-zero distribution of g-factors (Δg) caused the angular dependent line shape. Each different g-factor, expressed as g_i, within the distribution of g-factors shifts the magnetic field resonance. Typically, the resonances due to each g_i in g-strained systems are not resolved, and produce instead a linewidth that increases with frequency [105,120,121].

To test for non-zero g-strain in these samples, EPR spectroscopy beyond the standard X-band system is required. Microwave frequencies from 50-130 GHz were obtained from a single Network Analyzer as described in chapter 3 and a 7 T magnet was required to record the complete EPR spectrum at angles closest to 90^o. Figure 4.10 (a) shows EPR transmission spectra of the Mg-related signal with the c-axis oriented at 5^o and 40^o from the static magnetic field **B** at selected frequencies for free-standing GaN:Mg. The spectra shift horizontally, as expected, due to the frequency dependence of the resonance evident in Eq. 3.1. The increase of the linewidth with frequency seen by a comparison of the spectra measured at about 50 GHz (lower) with those measured around 100 GHz (upper) provides evidence of g-strain. Furthermore, the increase in linewidth at 40^o compared to that at 5^o reflects the greater sensitivity to non-axial strain expected for $\Delta g_\perp$ compared with $\Delta g_\parallel$ [84]. Samples with small non-uniform basal-crystal fields result in a large $\Delta g_\perp$ and a small $\Delta g_\parallel$ as seen in Figure 4.5 [84,96]. According to Equation 3.2, at angles close to 0^o, $\Delta g_\parallel$ will be weighted heavily in determining linewidth broadening while $\Delta g_\perp$ will have very little influence. The contribution from $\Delta g_\perp$ increases, and from $\Delta g_\parallel$ decreases, as the angle increases tends towards 90^o. Since a small $\Delta g_\parallel$ is predicted from

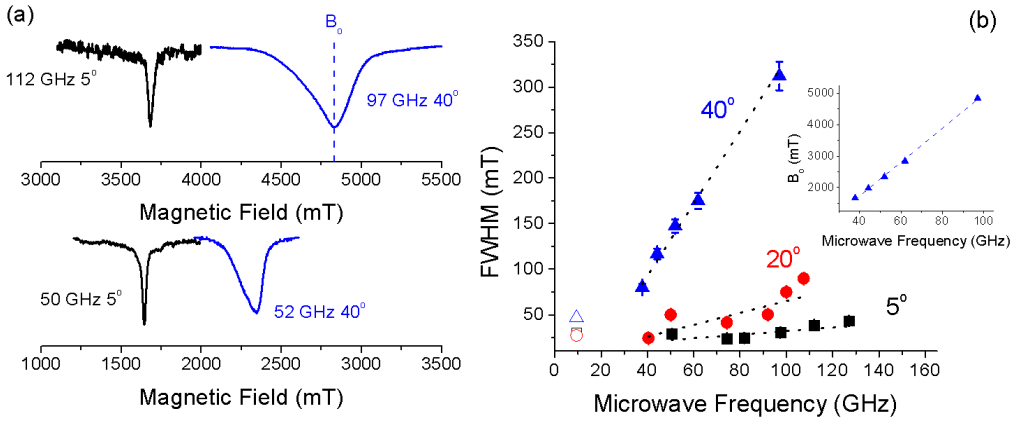

Figure 4.10 (a) EPR transmission spectra at 5° and 40° at two microwave frequencies and (b) frequency dependence of the FWHM of EPR spectra obtained from free-standing GaN:Mg measured with the angle between the c-axis and B : 5° (black squares), 20° (red circles), and 40° (blue triangles). Dashed lines are linear fits. Unfilled symbols are the X-band results, where the symbols follow the same legend as higher frequency data. The inset shows the peak magnetic field at resonance B_o as a function of microwave frequencies at 40°.

the crystal field model for small non-uniform basal crystal fields, the linewidth should be relatively frequency independent at low angles.

But as the angle increases $\Delta g_{\perp}$, which is expected to be more sensitive to non-uniform basal fields, will contribute more to the linewidth and the EPR signal will broaden with frequency. This trend is shown by the frequency dependence of the linewidth in Figure 4.10 (b). At 5° the linewidth is almost frequency independent, reflecting the influence of a very small $\Delta g_{\parallel}$. On the other hand, the linewidth varies linearly with frequency as the angle between the crystal c-axis and applied magnetic field increases, indicating increasing contributions from $\Delta g_{\perp}$. The frequency dependence of the linewidth shown in Fig. 4.9 (b) as well as the variation exhibited at different angles verifies the assumption of g-strain suggested by Zvanut et al., and provides further verification of the crystal field model suggested by Aliev et al. [83,87].

Included in the frequency-dependent data of Figure 4.10 (b) are three isolated points at 10 GHz. These data were obtained from the same samples measured at higher frequencies, but were measured in derivative mode using a conventional X-band spectrometer. Extrapolating from the data taken at higher frequencies suggests that the linewidth will not go through zero at 0 GHz, and that broadening mechanisms other than g-strain dominate at lower microwave frequencies. We suggest that a potential source of broadening is unresolved hyperfine splitting from neighboring Ga and N atoms. The delocalization of the hole wavefunction and the interaction strength with neighboring I = 1 N atoms and I = 3/2 Ga, each occurring with nearly 100% abundance, could ultimately determine the linewidth as the frequency is decreased, perhaps dominating at 10 GHz.

A likely culprit for the origin of g-strain in free-standing samples is the non-uniformity of defects. Potential fluctuations, caused by dislocations and ionized impurities, are present in all samples, causing spatially varying crystal fields. The variations in the crystal field splitting, which have both axial and basal components, will depend on the distance from each source of strain. If Mg is randomly distributed throughout a sample, each Mg can be affected by a different crystal field that depends on the distance from nearby defects, including dislocations or an interface. In thick free-standing samples with a low dislocation density, Mg will be affected on average by a smaller Δ_x and therefore a greater variation in $g_\perp$ will be observed [84]. The resulting EPR linewidth should be both anisotropic and frequency-dependent due to a large variation in g-factors within the sample, consistent with what is seen in free-standing crystals. If, however, the basal crystal field is large, as is predicted in thin-film samples due to a higher dislocation density and

interfacial lattice mismatch, small deviations of the basal crystal field should produce almost no variation in g-factors within the sample.

Frequency-dependent EPR measurements were attempted on thin-film MOVPE GaN:Mg samples but did not produce a resonance, possibly due to a reduced sensitivity in measurements. Thin-film samples were grown on mm-thick sapphire substrates, which do not provide any additional Mg EPR signal but do increase the filling factor of the resonant cavity and reduce the sensitivity of measurements i.e. reduce the Q-factor.

4.7 Alternative Frequency-Dependent Linewidth Mechanisms

The EPR frequency-dependent linewidth shown in section 4.6 provides substantial evidence for a non-uniform bi-axial crystal field Δ_x but there are alternative mechanisms that may also contribute to the same phenomena. In this section I discuss other possible physical processes that can also lead to an EPR frequency-dependent linewidth and their respective impact on the results shown in Figure 4.10.

4.7.1 Crystal curvature

Another potential explanation for the frequency-dependent linewidth, crystal curvature, was investigated. In g-factor anisotropic samples, crystal curvature can play a dominant role in EPR anisotropic linewidth broadening. Instead of all EPR centers oriented at one orientation with respect to the static magnetic field, as is the case of no sample curvature, there exists a distribution of orientations. Additionally, the sample c-axis is not completely in the same plane and now and a complete description of the crystal orientation requires both polar coordinates θ and φ that both vary due to crystal curvature, i.e. the sample is now at $\theta \pm \Delta\theta$, $\varphi \pm \Delta\varphi$. The distribution of orientations $\Delta\theta$, $\Delta\varphi$ will then

result in a distribution of g-factors Δg and cause an angular-dependent and frequency-dependent EPR linewidth broadening. The general g-factor resonance can be expressed from Eq. 2.7 as

$$g(\theta,\phi) = \left(g_{\perp}^{2}\sin^{2}\theta\sin^{2}\phi + g_{\parallel}^{2}\cos^{2}\theta\sin^{2}\phi + g_{\perp}^{2}\cos^{2}\phi +\right)^{1/2} \tag{4.2}$$

To approximate the distribution of orientations, X-ray diffraction (XRD) rocking curve measurements were obtained across a 14 mm length, focusing the x-ray beam path at each of the red circles along the sample as shown in Figure 3.2 for an HVPE sample. By measuring the shift in the rocking curve peak, a function of the x-ray beam position on the sample the radius of curvature, can be determined [99]. The angular distribution can be determined from the arc length equations

$$\Delta\theta = \frac{W}{R} \tag{4.3}$$

$$\Delta\phi = \frac{L}{R} \tag{4.4}$$

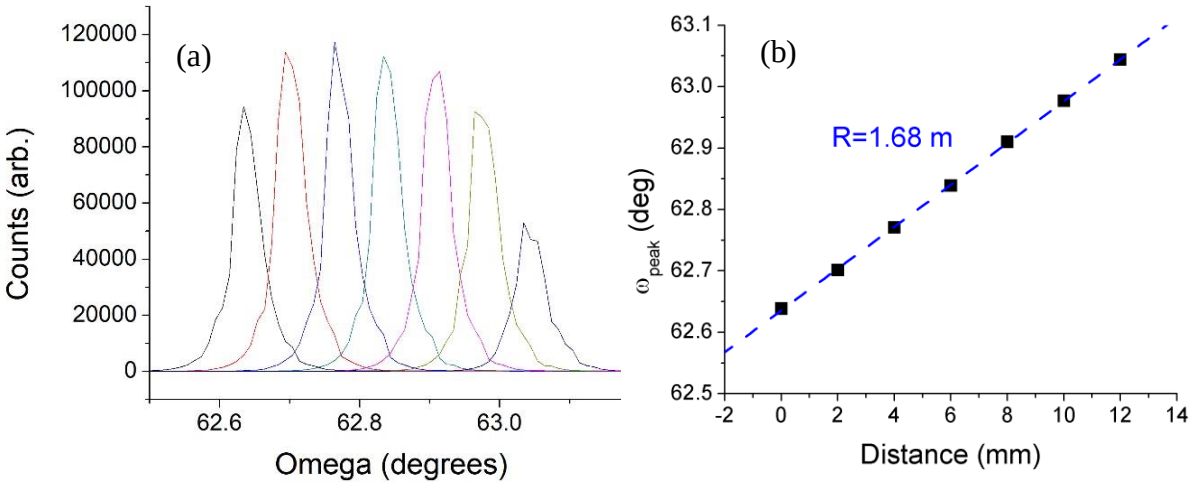

Figure 4.11. (a) Rocking curve spectra from (006) plane at different points on the sample. (b) Peak position, ω_{peak}, of rocking curve as position of distance across sample. The slope is proportional to the radius of curvature.

where R is the radius of curvature and L and W are the length and width of a sample, respectively. From performing a rocking curve measured at discrete points on a sample, shown in Figure 3.1, the diffraction peak was observed to shift, shown in Figure 4.11 (a). From a linear fit shown in Figure 4.11 (b) it was determined that the radius of curvature is 1.7 m for the free-standing HVPE samples and nearly 12 m for the thin-films, which is not shown. With sample dimensions known and taking the differential of Eq. 4.1 w.r.t. θ and ϕ, the angular dependent linewidth from crystal curvature can now be quantified via Eq. 3.6, which is frequency dependent. The crystal curvature was found to contribute no more than 3% to the slope of the frequency dependent linewidth at 40^{o}. This information is highlighted in Table 4.4 showing the experimental frequency-dependent linewidth and the corresponding contribution due to crystal curvature as a function of angle.

Table 4.4. The rate of which the Mg-related EPR signal linewidth was observed to change with microwave frequency and the corresponding influence from crystal bowing at selected orientations of the crystal c-axis with the external magnetic field B for free-standing HVPE samples.

Angle (Degrees)	Experimental mT/GHz	Crystal Bowing mT/GHz
5	0.2 ± 0.1	0.01
20	0.65 ± 0.2	0.025
40	4 ± 0.3	0.1

4.7.2 Generalization of the bi-axial crystal field direction

Another mechanism for a frequency-dependent EPR linewidth is generalizing the bi-axial crystal field direction Hamiltonian used to determine g-factors. Up until this point, the variation in the magnitude of a crystal field in the x-direction Δ_x modeled the observed g-factors in samples. In reality, there is no logical reason to assume that a bi-axial crystal field exists only along the x-direction. To correct for this, we transform the bi-axial crystal field Hamiltonian term to

$$\Delta_x\left(\hat{L}_x^2 - L(L+1)/3\right) \longrightarrow \Delta_\perp\left(\hat{L}_\perp^2 - L(L+1)/3\right)$$
$$\hat{L}_\perp = \hat{L}_x \cos\beta + \hat{L}_y \sin\beta \tag{4.5}$$

Where β is the bi-axial crystal field angle for a specific defect. If β is allowed to vary from defect sites, each value of β will create a different g-factor, causing g-strain and therefore a frequency-dependent linewidth. J.J. Davies determined that, at large crystal fields, the variation in $g_\perp$ is seen to be appreciably large ($\Delta g_\perp$~0.02) [122]. Small crystal fields, however, have a very small variation of $g_\perp$ ($\Delta g_\perp < 0.001$) as is seen in Figure 4.12. From the variance of g, a frequency-dependent linewidth can again be calculated from this

phenomenon. Comparing to the highest angle, and therefore largest contribution to the frequency-dependent linewidth, at 40°, the variation in g is calculated to be less than $1x10^{-4}$, resulting in a frequency dependent linewidth contribution of less than 1% of what is observed for free-standing samples. Therefore, a varying bi-axial crystal field direction cannot explain either the frequency-dependent or angular-dependent linewidth observed in free-standing samples.

Thin-film samples, however, can have a significant contribution to their angular-dependent change in linewidth due to the variation in bi-axial crystal field directions. When the bi-axial crystal field is large, i.e. in thin-film samples ,variations in the crystal field direction results in $g_\perp$ varying 0.01-0.02, which for MOVPE g-factor parameters taken from Table 4.3, results in a linewidth increase of 15% when rotating from 0° to 90°. Thus, the linewidth change observed in MOVPE thin-films can readily be explained by an application of a more generalized bi-axial crystal field direction. In MME samples, the

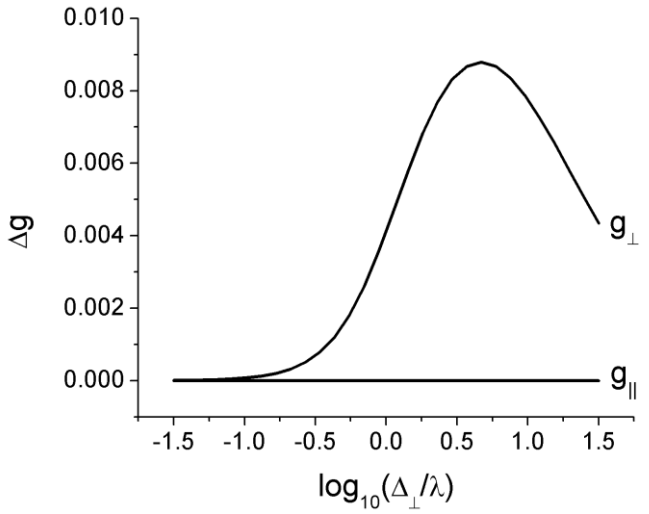

Figure 4.12 Variation in g-factor from generalizing the bi-axial crystal field Hamiltonian term to $\Delta_x \rightarrow \Delta_\perp$ as specified in Eq. 4.5.

magnitude of the bi-axial crystal field is so large that variations in the bi-axial crystal field direction provide no g-strain, and thus no change in linewidth nor lineshape, implying from Figure 4.12 that $\Delta_{\perp}/\lambda > 1.5$.

4.8 Temperature Dependence

The temperature dependence of an EPR transition is an additional parameter that can be varied to extract information about a defect center. Additional thermal energy supplied to the crystal and paramagnetic center can change the structure of the defect, such as the local symmetry or spin relaxation dynamics, and result in changes in the EPR spectra. To effectively model the EPR results for the Mg^0 acceptor, the spin-orbit coupling λ and orbital reduction factor g_l was required to be significantly reduced from the atomic values of -15 meV and 1, respectively. This section specifically deals with the temperature dependence of the Mg^0 acceptor and discusses the reduced λ and g_l values.

4.8.1 Temperature dependence and the Jahn-Teller effect

The temperature dependence of both thin-film and free-standing samples were measured from 3.5 – 25 K. The EPR intensity of each sample varies inversely with respect to temperature, as is expected from the Boltzmann distribution of spins. The peak-to-peak linewidth (B_{pp}) dependence on temperature is not as straightforward. To compare the change in EPR linewidth with temperature on the same scale, all changes in linewidth are compared to their respective 3.5 K linewidth, as is shown in Figure 4.13. Thin-film samples were oriented at 30^o and free-standing HVPE samples at 20^o to achieve a symmetric linewidth. From 3.5 - 25 K, the EPR linewidth from thin-film samples (purple crosses) changed less than 1 ± 0.4 mT, about 10% of the 3.5 K linewidth. Additionally,

the g-factor was seen to change less than 0.02. For free-standing samples (black squares, red circles, blue triangles, and green stars), however, the peak-to-peak linewidth varied significantly with respect to a change in temperature. There is also evidence that the g-factor in free-standing HVPE samples is temperature dependent; future work is required to further study the g-factor dependence on temperature. As the temperature increases from 3.5 to 6 K, the linewidth increases monotonically for the free-standing samples. Above 7 K, the signal intensity in free-standing samples was too small to extract a meaningful linewidth.

It is very common in the literature to attribute a linewidth change in temperature directly to a temperature dependent spin-lattice relaxation [94]. To first order, the spin-lattice relaxation is typically modeled as a dynamic crystal field coupling that facilitates the energy transfer from an excited spin to the surrounding lattice [123]. Although possible, there have been no reports of a linewidth changing so significantly in such a short temperature range due to spin-lattice effects– over 10 mT peak-to-peak in 2.5 K. Such a dramatic change in relaxation time in this temperature range would require a significant change in Mg^0 phonon-spin coupling with temperature, which has not been reported in the literature.

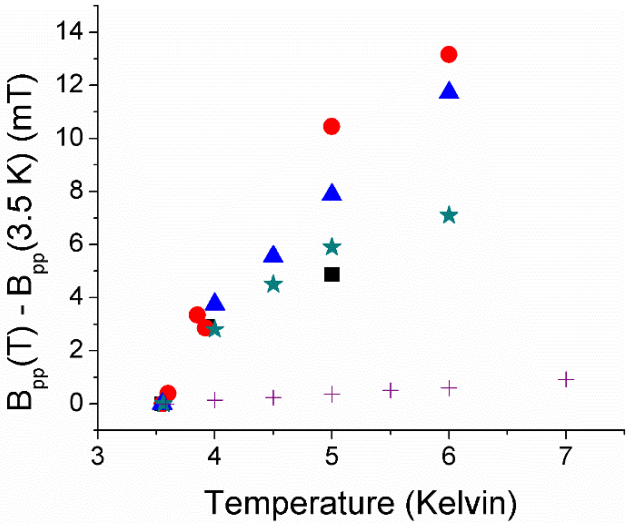

Figure 4.13. Change in Lorentzian 9.4 GHz EPR linewidth of Mg-related signal for a thin-film MOVPE (purple cross) sample and free-standing HVPE samples with Mg concentrations of $4x10^{17}$ (black squares), $1.5x10^{18}$ (red circles), $3x10^{18}$ (blue triangles), and $6x10^{18}$ (green stars) cm^{-3} oriented at 20° for free-standing samples and 30° for thin-film samples.

Below is a possible explanation for the temperature dependent phenomena that is also consistent with the crystal field model presented in the previous results and discussion. Previous DFT calculations have determined that one of the possible ground states for the Mg hole localization on a basal nitrogen neighbor. In this model there are three equivalent basal nitrogen atoms (B) for localization, indicated by the schematic in Figure 1.2 (b) [77]. From the papers of Jahn and Teller, when a non-linear complex is orbitally degenerate, i.e. the energies of at least two states are the same and their only difference is in the orbital wavefunction component, the system is unstable and will undergo a nuclear distortion which will break the degeneracy and further lower the energy of the system [124,125]. If the coupling between the electrons and the distortion is weak relative to the zero-point energy of the associated vibrational modes or if the vibrational mode is comparable to the barrier separating equivalent configurations, then there will be coupled motion between the

vibrational modes and electrons. This is the dynamic Jahn Teller (DJT) effect. Since localization of the hole on each of the basal nitrogen atoms have the same energy but different spatial localization then, according to the Jahn-Teller theorem, the system must undergo a local asymmetric nuclear distortion in order to break the degeneracy [126]. It has been shown that the hopping frequency between equivalent Jahn-Teller (JT) distortions is temperature dependent and can lead to EPR linewidth broadening and g-factor shifts over small temperature ranges [127].

The hopping frequency f_{re} at a given temperature is exponentially dependent on the energy barrier between equivalent configurations, δ_{JT}, and if the correlation time between reorientations is much shorter than the modulation frequency ($1/f_{re}<10^{-7}$ s), the EPR transition will become lifetime broadened [127,128]. Authors have been able to determine δ_{JT} from temperature dependent EPR measurements assuming the linewidth broadening mechanism is dominated by Jahn-Teller reorientation hopping [127]. By assuming the temperature dependent linewidth broadening quantified in Figure 4.13 is a direct result of the Mg^0 hole reorienting between equivalent basal N sites in free-standing GaN, the reorientation barrier δ_{JT} was calculated to be $\delta_{JT} \approx 0.5$ meV. As a comparison, the NV center in diamond is calculated by DFT to be ~9 meV, and 60 meV for the Si E-center - substantially larger than the value obtained here. Although the δ_{JT} determined from the measurements is small, numbers similar in magnitude have been reported in other systems, with $\delta_{JT} = 0.6$ meV for Eu^{2+} in alkaline earth fluorides [129].

Another component of equivalent Jahn-Teller distorted systems is that each defect center has several symmetry-related sites that are oriented uniquely within the crystal, giving rise to a potentially different g-factor angular dependence [127]. In GaN, each Ga

and N has the same tetrahedral coordination, but their bond angles are rotated by 60° in the c-plane, giving rise to six possible unique orientations for the Mg_{Ga} hole localized on a basal neighbor N yet only one transition is seen from EPR. To explain the phenomena of seeing only one signal, we attempt to model potential static Jahn-Teller distortions and calculate the resulting g-factor anisotropy. By applying a crystal field along basal N-bonds Δ_ζ with the additional spin-orbit coupling and axial crystal field terms, the g-factor angular dependence for each basal localization can be determined for a given magnitude of Δ_ζ [122]. The resulting variation of g-factors are unsurprisingly similar to the results reported in Figure 4.11, with free-standing samples having a Δg of less than 0.01, resulting in EPR transitions that are less than 1 mT apart, and lead to multiple unresolved transitions merged into one signal.

The DJT also must be discussed in heteroepitaxial thin-film samples that have a temperature-independent linewidth. When the bi-axial crystal field is large, as is the case in thin-film and ammonothermal samples, the tunneling probability between vibronic states will be reduced and the distortion will now be static [127,128,130]. Since there will be no vibronic coupling in the static JT case and therefore no hopping between symmetry sites, there should be no observed temperature dependent linewidth broadening, as was observed in thin-film samples shown in Figure 4.13.

4.8.2 A discussion of reduced Hamiltonian parameters g_l and λ

The orbital reduction factor, noted as g_l in this text, is reduced from unity to account for an increased delocalization of an electron, often described as an increased covalency. $g_l < 1$ is required to effectively model the g-factor anisotropy observed for the Mg acceptor

in section 4.1. Two possible origins of $g_l < 1$ are discussed below: the formation of extended molecular orbitals and a dynamic Jahn-Teller (DJT) effect.

In the work of Stevens, it was shown that the mixing of atomic d and ligand p orbitals can be simplified by using only the atomic d-orbitals and replacing the operator **L** by g_l**L** [131]. By modifying the operator **L** to g_l**L**, both the orbital component of the magnet moment $\boldsymbol{\mu}_L = \mu_B g_l \boldsymbol{L}$ and the spin-orbit coupling $g_l\lambda$**LS** are altered. When molecular orbitals are included, the value of g_l is determined exclusively by the amount of atomic--ligand and ligand-ligand wavefunction overlap and the atomic spin-orbit coupling constant λ [92].

The second mechanism for reducing g_l, the dynamic Jahn-Teller effect originates from a weak orbital degeneracy distortion [103]. This coupling of states with different orbital components creates a delocalized wavefunction. The DJT coupling reduces g_l and, additionally, lowers the spin-orbit coupling strength λ [Frank Ham 1965]. Unlike in the first example with delocalized molecular wavefunctions, the states being considered can be exclusively atomic.

The orbital reduction from either of the above-mentioned mechanism quenches the orbital angular momentum contribution to g-factor anisotropy, as seen in Eq. 3.4. Currently in Mg^0, g_l is determined by fitting the g-factor anisotropy to experimental data. Computational methods allow for determining g_l by calculating the electron-phonon coupling [132]. Currently, computational g_l results do not exist for the Mg^0 acceptor, but spin-density visualizations for a basal-oriented ground state suggest that g_l and λ will be reduced [77].

CHAPTER 5

CONCLUSIONS

5.1 Summary of Results

In this work, I provide evidence from electron paramagnetic resonance experiments that supports the model for the Mg acceptor as a hole on a basal site in GaN. By the application of crystal field theory, the magnitude of the bi-axial crystal field was shown to play a pivotal role in the Mg^0 paramagnetic characteristics. Electronic devices, such as field effect transistors, are dependent on high hole mobility. Also, two-dimensional confinement requires small bi-axial crystal fields, which impact performance. Currently, Mg is viewed as the sole successful p-type dopant in GaN . By measuring the EPR Mg^0 characteristics, a qualitative assessment of the bi-axial crystal field local to the Mg acceptor can be determined, assisting in device design.

The GaN:Mg samples studied varied significantly in several features: the Mg concentration ranged from $4x10^{17}$-2x20 cm^{-3}, threading dislocations varied from $5x10^4$-10^{10} cm^{-2}, and the thickness from 0.4-1000 µm. This wide range of parameters was possible due to the many growth methods (MOVPE, MME, HVPE, ammothermal) available and allowed for the study of heteroepitaxial thin-film and thick, free-standing samples. Homoepitaxial grown ammonothermal samples, which contained high concentrations of compensated O donors, were also included in this study and provided an additional test to the crystal field method for the Mg acceptor in GaN.

10 GHz EPR measurements at 3.5 K identified the EPR related Mg^0 signal in all GaN:Mg samples with the best fit g-factors listed in Table 4.1. The g-factor anisotropy was observed to be dependent on Mg concentration and Al alloying concentration. Mechanical strain from different threading dislocation densities and substrate-film interface also played a pivotal role in determining the g-factor, intensity, and lineshape anisotropy.

The following summarizes the main significance of this work:

1. A crystal field model employing biaxial strain was tested using the wide range of samples described above and in section 3.1.

2. In most samples, the magnitude of Δ_x is determined by physical strain mechanisms, e.g. dislocation density, alloying concentration, or impurity concentration. In free-standing homoepitaxial grown ammonothermal samples, which have significantly reduced bulk strain, however, the crystal field is caused by the large concentration of ionized donor sites.

3. The model correctly predicted that, despite the small strain in ammonothermal samples, not only would the g-factor anisotropy be reduced as predicted by Aliev et al., but also the intensity anisotropy would be reduced [84]. Additionally, the Mg hole was determined to be on basal sites by examining the EPR angular dependent intensity in thin-film and free-standing samples. When the Mg hole is modelled to be on an axial N neighbor, the predicted anisotropic intensity is severely underestimated and does not agree with experimental results.

4. Non-uniformities in the bi-axial crystal field are shown to be present in free-standing HVPE samples from the lineshape anisotropy, consistent with the

basal-N model. In free-standing HVPE samples, small variations of Δ_x can result in large variations of $g_\perp$ ($\Delta g_\perp$) but only a small distribution of $g_\parallel$ ($\Delta g_\parallel$) and dictate the angular dependent lineshape. Frequency-dependent EPR measurements confirmed the linear dependence of linewidth on the microwave frequency predicted by the non-axial crystal field.

5. The anisotropic lineshape observed in some thin-film samples are not caused by non-uniformity of the magnitude of Δ_x. Instead, the in-plane direction of the bi-axial crystal field, i.e. $\Delta_x \longrightarrow \Delta_\perp$ affects the angular dependent lineshape.

6. The Mg-related EPR signal was observed to be temperature dependent in free-standing HVPE samples, increasing by nearly a factor of 2 over a range of 2.5 K which is consistent with the basal-N crystal field model. This significant change in linewidth could be evidence of the Mg acceptor hopping over a small energy barrier between equivalent basal N neighbor sites. The orbital reduction factor g_l and spin-orbit coupling constant λ are consistent with the small magnitude of the energy barrier.

5.2 Future Work

Throughout much of this work, I attempt to be particularly careful with specifying the EPR signal associated with the Mg acceptor as the "Mg-related EPR signal" and in the Results and Discussion chapter 4 I am able to merely conclude that the Mg acceptor hole is on a basal site. I use these non-specific terms out of necessity, as my EPR measurements have been unable to conclude a specific site localization of the Mg acceptor. Most commonly in EPR spectroscopy, the localization of a paramagnetic center can be

determined from the neighboring nuclei, which provide hyperfine and superhyperfine interaction terms into the spin Hamiltonian. The Mg-related EPR signal, to date, has shown no evidence of resolved nuclear interactions but is suspected to be a dominant source of the 10-15 mT peak-to-peak linewidth. Other experimental techniques have also been unsuccessful in local structure determination. Therefore, the only knowledge to the specifics of hole localization is from computational DFT. Described below are a few proposed experiments, with varying success rates predicted, that have the potential of revealing more information about local Mg acceptor interactions in GaN.

5.2.1 ENDOR spectroscopy

When a magnetic resonance scientist hears the words "potential unresolved hyperfine", the technique Electron Nuclear DOuble Resonance (ENDOR) most likely pops into their mind. In ENDOR experiments, by saturating an EPR transition with microwaves, the spin system is then subjected to radio frequency photons in an attempt to change the nuclear spin population. By observing the change in EPR signal intensity as the nuclear spin population changes, precise electron-nuclear couplings can be observed. With $I = 1$ for N in 100% abundance and $I = 3/2$ for Ga with two isotopes, the expected ENDOR spectra will be full of spectroscopic information, most notably hyperfine coupling strengths. The chance of success for ENDOR experiments is questionable, as the spectroscopy has relatively low sensitivity. However, if resonance is observed then there should be extremely valuable information pertaining to the localization of the Mg acceptor.

5.2.2 Lower temperature EPR measurements

Lower temperature cw-EPR measurements also have a potential for revealing additional structure to the broad S=1/2 transition. From an experimental point of view, temperatures of 1.5 K in EPR measurements have been achieved by pumping on the liquid He. Although a change in 2 K might seem unimpressive, from Figure 4.12 (a) in section 4.8, we observed that the peak-to-peak linewidth of the Mg-related EPR signal in HVPE free-standing samples was very sensitive to temperature and increased by nearly 100% in a 2.5 K range from 3.5-6 K. Linearly extrapolating this linewidth trend, decreasing the temperature below 3.5 K should further decrease the peak-to-peak linewidth to less than 5 mT and potentially reveal additional information about the Mg acceptor. Of all the proposed future work, I would suggest this one as the most promising, as it does not require a lot of experimental equipment and is relatively inexpensive.

LIST OF REFERENCES

[1] Masui H, Nakamura S, DenBaars S P and Mishra U K 2010 Nonpolar and Semipolar III-Nitride Light-Emitting Diodes: Achievements and Challenges *IEEE Trans. Electron Devices* **57** 88–100

[2] DenBaars S P, Feezell D, Kelchner K, Pimputkar S, Pan C-C, Yen C-C, Tanaka S, Zhao Y, Pfaff N, Farrell R, Iza M, Keller S, Mishra U, Speck J S and Nakamura S 2013 Development of gallium-nitride-based light-emitting diodes (LEDs) and laser diodes for energy-efficient lighting and displays *Acta Mater.* **61** 945–51

[3] Tompkins R P, Smith J R, Kirchner K W, Jones K A, Leach J H, Udwary K, Preble E, Suvarna P, Leathersich J M and Shahedipour-Sandvik F 2014 GaN Power Schottky Diodes with Drift Layers Grown on Four Substrates *J. Electron. Mater.* **43** 850–6

[4] Jessen G H, Fitch R C, Gillespie J K, Via G, Crespo A, Langley D, Denninghoff D J, Trejo M and Heller E R 2007 Short-Channel Effect Limitations on High-Frequency Operation of AlGaN/GaN HEMTs for T-Gate Devices *IEEE Trans. Electron Devices* **54** 2589–97

[5] Tomiya S, Hino T, Goto S, Takeya M and Ikeda M 2004 Dislocation related issues in the degradation of GaN-based laser diodes *IEEE J. Sel. Top. Quantum Electron.* **10** 1277–86

[6] Marino F A, Faralli N, Palacios T, Ferry D K, Goodnick S M and Saraniti M 2010 Effects of threading dislocations on AlGaN/GaN high-electron mobility transistors *IEEE Trans. Electron Devices* **57** 353–60

[7] Götz W, Johnson N M, Walker J, Bour D P and Street R a. 1996 Activation of acceptors in Mg-doped GaN grown by metalorganic chemical vapor deposition *Appl. Phys. Lett.* **68** 667

[8] Nakarmi M L, Nepal N, Lin J Y and Jiang H X 2009 Photoluminescence studies of impurity transitions in Mg-doped AlGaN alloys *Appl. Phys. Lett.* **94** 091903

[9] Dreyer C E, Janotti A and Van de Walle C G 2013 Effects of strain on the electron effective mass in GaN and AlN *Appl. Phys. Lett.* **102** 142105

[10] Kaufmann U, Schlotter P, Obloh H, Köhler K and Maier M 2000 Hole conductivity and compensation in epitaxial GaN:Mg layers *Phys. Rev. B - Condens. Matter Mater. Phys.* **62** 10867–72

[11] Miceli G and Pasquarello A 2016 Self-compensation due to point defects in Mg-doped GaN *Phys. Rev. B* **93** 165207

[12] Sasangka W A, Syaranamual G J, Made R I, Thompson C V. and Gan C L 2016 Threading dislocation movement in AlGaN/GaN-on-Si high electron mobility transistors under high temperature reverse bias stressing *AIP Adv.* **6**

[13] Schmidt T H, Siebert M, Flege J I, Figge S, Gangopadhyay S, Pretorius A, Lee T L, Zegenhagen J, Gregoratti L, Barinov A, Rosenauer A, Hommel D and Falta J 2011 Mg and Si dopant incorporation and segregation in GaN *Phys. Status Solidi Basic Res.* **248** 1810–21

[14] Cruz S C, Keller S, Mates T E, Mishra U K and DenBaars S P 2009 Crystallographic orientation dependence of dopant and impurity incorporation in GaN films grown by metalorganic chemical vapor deposition *J. Cryst. Growth* **311** 3817–23

[15] Bergman P, Ying G, Monemar B and Holtz P O 1987 Time-resolved spectroscopy of Zn- and Cd-doped GaN *J. Appl. Phys.* **61** 4589–92

[16] Nakano Y and Jimbo T 2002 Electrical characterization of acceptor levels in Be-implanted GaN *Appl. Phys. Lett.* **81** 3990–2

[17] Kucheyev S ., Williams J . and Pearton S . 2001 Ion implantation into GaN *Mater. Sci. Eng. R Reports* **33** 51–108

[18] Gaskill D K, Brandt C D and Nemanich R J 1996 III-Nitride, SiC and Diamond Materials for Electronic Devices. Symposium Held April 8-12 1996, San Francisco, California, U.S.A. Volume 423.

[19] Palacios T, Chakraborty A, Rajan S, Poblenz C, Keller S, DenBaars S P, Speck J S and Mishra U K 2005 High-power AlGaN/GaN HEMTs for Ka-band applications *IEEE Electron Device Lett.* **26** 781–3

[20] Maruska H P and Tietjen J J 1969 The Preparation and properties of vapor-deposited single-crystalline GaN *Appl. Phys. Lett.* **15** 327–9

[21] Nakamura S, Senoh M, Mukai T, Transistors H B, Makimoto T, Kido T, Guangrui Y and Guanghan F 1991 GaN Growth Using GaN Buffer Layer *Jpn. J. Appl. Phys.* **30** L1705–7

[22] Amano H, Sawaki N, Akasaki I and Toyoda Y 1986 Metalorganic vapor phase epitaxial growth of a high quality GaN film using an AlN buffer layer *Appl. Phys. Lett.* **48** 353–5

[23] Götz W, Johnson N M, Bour D P, McCluskey M D and Haller E E 1996 Local vibrational modes of the Mg–H acceptor complex in GaN *Appl. Phys. Lett.* **69** 3725–7

[24] Hiroshi A, Masahiro K, Kazumasa H and Isamu A 1989 P-Type Conduction in Mg-Doped GaN Treated with Low-Energy Electron Beam Irradiation (LEEBI) *Jpn. J. Appl. Phys.* **28** L2112

[25] Nakamura S, Mukai T, Senoh M and Iwasa N 1992 Thermal Annealing Effects on P-Type Mg-Doped GaN Films *Jpn. J. Appl. Phys.* **31** L139–42

[26] Jones E A, Wang F F and Costinett D 2016 Review of Commercial GaN Power Devices and GaN-Based Converter Design Challenges *IEEE J. Emerg. Sel. Top. Power Electron.* **4** 707–19

[27] Nakamura S and Krames M R 2013 History of Gallium–Nitride-Based Light-Emitting Diodes for Illumination *Proc. IEEE* **101** 2211–20

[28] Kozodoy P, Keller S, DenBaars S . and Mishra U . 1998 MOVPE growth and characterization of Mg-doped GaN *J. Cryst. Growth* **195** 265–9

[29] Huang W-C, Chu C-M, Wong Y-Y, Chen K-W, Lin Y-K, Wu C-H, Lee W-I and Chang E-Y 2016 Investigations of GaN growth on the sapphire substrate by MOCVD method with different AlN buffer deposition temperatures *Mater. Sci. Semicond. Process.* **45** 1–8

[30] Burnham S D, Namkoong G, Look D C, Clafin B and Doolittle W A 2008 Reproducible increased Mg incorporation and large hole concentration in GaN using metal modulated epitaxy *J. Appl. Phys.* **104** 024902

[31] Heinke H, Kirchner V, Einfeldt S and Hommel D 2000 X-ray diffraction analysis of the defect structure in epitaxial GaN *Appl. Phys. Lett.* **77** 2145–7

[32] Park H J, Park C, Yeo S, Kang S W, Mastro M, Kryliouk O and Anderson T J 2005 Epitaxial strain energy measurements of GaN on sapphire by Raman spectroscopy *Phys. Status Solidi C Conf.* **2** 2446–9

[33] Sugahara T, Sato H, Hao M, Naoi Y, Kurai S, Tottori S, Yamashita K, Nishino K, Romano L T and Sakai S 1998 Direct Evidence that Dislocations are Non-Radiative Recombination Centers in GaN *Jpn. J. Appl. Phys.* **37** L398–400

[34] Marino F A, Faralli N, Palacios T, Ferry D K, Goodnick S M and Saraniti M 2010 Effects of Threading Dislocations on AlGaN/GaN High-Electron Mobility Transistors *IEEE Trans. Electron Devices* **57** 353–60

[35] Sugiura L 1997 Dislocation motion in GaN light-emitting devices and its effect on device lifetime *J. Appl. Phys.* **81** 1633–8

[36] Williams A D and Moustakas T D 2007 Formation of large-area freestanding gallium nitride substrates by natural stress-induced separation of GaN and sapphire *J. Cryst. Growth* **300** 37–41

[37] Zvanut M E, Dashdorj J, Freitas J A, Glaser E R, Willoughby W R, Leach J H and Udwary K 2016 Incorporation of Mg in Free-Standing HVPE GaN Substrates *J. Electron. Mater.* **45** 2692–6

[38] Leszczynski M, Teisseyre H, Suski T, Grzegory I, Bockowski M, Jun J, Porowski S, Pakula K, Baranowski J M, Foxon C T and Cheng T S 1996 Lattice parameters of gallium nitride *Appl. Phys. Lett.* **69** 73–5

[39] GaN Wurtzie crystal structure [Online]. https://en.wikipedia.org/wiki/File:Wurtzite_polyhedra.png.

[40] Bernardini F, Fiorentini V and Vanderbilt D 1997 Spontaneous polarization and piezoelectric constants of III-V nitrides *Phys. Rev. B* **56** R10024–7

[41] Vurgaftman I, Meyer J R and Ram-Mohan L R 2001 Band parameters for III-V compound semiconductors and their alloys *J. Appl. Phys.* **89** 5815–75

[42] Misra P, Behn U, Brandt O, Grahn H T, Imer B, Nakamura S, Denbaars S P and Speck J S 2006 Polarization anisotropy in GaN films for different nonpolar orientations studied by polarized photoreflectance spectroscopy *Appl. Phys. Lett.* **88**

[43] Lee L Y 2017 Cubic zincblende gallium nitride for green-wavelength light-emitting diodes *Mater. Sci. Technol. (United Kingdom)* **33** 1570–83

[44] Khromov S, Hemmingsson C G, Amano H, Monemar B, Hultman L and Pozina G 2011 Luminescence related to high density of Mg-induced stacking faults in homoepitaxially grown GaN *Phys. Rev. B - Condens. Matter Mater. Phys.* **84** 3–8

[45] Oliver R A, Kappers M J, Sumner J, Datta R and Humphreys C J 2006 Highlighting threading dislocations in MOVPE-grown GaN using an in situ treatment with SiH4 and NH3 *J. Cryst. Growth* **289** 506–14

[46] Götz W, Johnson N M, Chen C, Liu H, Kuo C and Imler W 1996 Activation energies of Si donors in GaN *Appl. Phys. Lett.* **68** 3144–6

[47] Liu S T, Yang J, Zhao D G, Jiang D S, Liang F, Chen P, Zhu J J, Liu Z S, Li X, Liu W, Zhang L Q, Long H and Li M 2017 Different annealing temperature suitable for different Mg doped P-GaN *Superlattices Microstruct.* **104** 63–8

[48] Hu H, Zhou S, Wan H, Liu X, Li N and Xu H 2019 Effect of strain relaxation on performance of InGaN/GaN green LEDs grown on 4-inch sapphire substrate with sputtered AlN nucleation layer *Sci. Rep.* **9** 3447

[49] Lee S R, West A M, Allerman A A, Waldrip K E, Follstaedt D M, Provencio P P, Koleske D D and Abernathy C R 2005 Effect of threading dislocations on the Bragg peakwidths of GaN, AlGaN, and AlN heterolayers *Appl. Phys. Lett.* **86** 241904

[50] Gay P, Hirsch P . and Kelly A 1953 The estimation of dislocation densities in metals from X-ray data *Acta Metall.* **1** 315–9

[51] Perlin P, Camassel J, Knap W, Taliercio T, Chervin J C, Suski T, Grzegory I and Porowski S 1995 Investigation of longitudinal-optical phonon-plasmon coupled modes in highly conducting bulk GaN *Appl. Phys. Lett.* **67** 2524–6

[52] Perlin P, Jauberthie-Carillon C, Itie J P, San Miguel A, Grzegory I and Polian A 1992 Raman scattering and x-ray-absorption spectroscopy in gallium nitride under high pressure *Phys. Rev. B* **45** 83–9

[53] Fletcher J S and Vickerman J C 2013 Secondary Ion Mass Spectrometry: Characterizing Complex Samples in Two and Three Dimensions *Anal. Chem.* **85** 610–39

[54] Reshchikov M A and Morkoç H 2005 Luminescence properties of defects in GaN *J. Appl. Phys.* **97** 061301

[55] Van De Walle C G and Neugebauer J 2004 First-principles calculations for defects and impurities: Applications to III-nitrides *J. Appl. Phys.* **95** 3851–79

[56] Angeles J, Antonelli G, Arai F, Arbib M A, Angeles L, Bicchi A, Billard A, Algorithms L, Billingsley J, Book W, Breazeal C, Brock O and Broggi A 2000 III-Nitride Semiconductors: Electrical, Structural and Defects Properties *Methods Cell Sci.* **22** 25

[57] Lyons J L and Van de Walle C G 2017 Computationally predicted energies and properties of defects in GaN *npj Comput. Mater.* **3** 12

[58] Saarinen K, Seppälä P, Oila J, Hautojärvi P, Corbel C, Briot O and Aulombard R L 1998 Gallium vacancies and the growth stoichiometry of GaN studied by positron annihilation spectroscopy *Appl. Phys. Lett.* **73** 3253–5

[59] Chow K H, Vlasenko L S, Johannesen P, Bozdog C, Watkins G D, Usui A, Sunakawa H, Sasaoka C and Mizuta M 2004 Intrinsic defects in GaN.I.Ga sublattice defects observed by optical detection of electron paramagnetic resonance *Phys. Rev. B - Condens. Matter Mater. Phys.* **69** 1–9

[60] Son N T, Hemmingsson C G, Paskova T, Evans K R, Usui A, Morishita N, Ohshima T, Isoya J, Monemar B and Janzén E 2009 Identification of the gallium vacancy-oxygen pair defect in GaN *Phys. Rev. B - Condens. Matter Mater. Phys.* **80** 2–5

[61] Von Bardeleben H J, Cantin J L, Vrielinck H, Callens F, Binet L, Rauls E and Gerstmann U 2014 Nitrogen split interstitial center (N- N) N in GaN: High frequency EPR and ENDOR study *Phys. Rev. B - Condens. Matter Mater. Phys.* **90** 1–12

[62] Götz W, Johnson N M, Chen C, Liu H, Kuo C and Imler W 1996 Activation energies of Si donors in GaN *Appl. Phys. Lett.* **68** 3144–6

[63] Obloh H, Bachem K ., Kaufmann U, Kunzer M, Maier M, Ramakrishnan A and Schlotter P 1998 Self-compensation in Mg doped p-type GaN grown by MOCVD *J. Cryst. Growth* **195** 270–3

[64] Carlos W E, Freitas J A, Khan M A, Olson D T and Kuznia J N 1993 Electron-spin-resonance studies of donors in wurtzite GaN *Phys. Rev. B* **48** 17878–84

[65] Wolos A, Wilamowski Z, Piersa M, Strupinski W, Lucznik B, Grzegory I and Porowski S 2011 Properties of metal-insulator transition and electron spin relaxation in GaN:Si *Phys. Rev. B* **83** 165206

[66] Wickramaratne D, Shen J X, Dreyer C E, Engel M, Marsman M, Kresse G, Marcinkevičius S, Alkauskas A and Van de Walle C G 2016 Iron as a source of efficient Shockley-Read-Hall recombination in GaN *Appl. Phys. Lett.* **109**

[67] Chisholm J A and Bristowe P D 2001 Formation energies of metal impurities in GaN *Comput. Mater. Sci.* **22** 73–7

[68] Maier K, Kunzer M, Kaufmann U, Schneider J, Monemar B, Akasaki I and Amano H 1993 Iron Acceptors in Gallium Nitride (GaN) *Mater. Sci. Forum* **143**–**147** 93–8

[69] Baranov P G, Ilyin I V, Mokhov E N and Roenkov A D 1996 Identification of manganese trace impurity in GaN crystals by electron paramagnetic resonance *Semicond. Sci. Technol.* **11** 1843–6

[70] Palczewska M, Wolos A, Kaminska M, Grzegory I, Bockowski M, Krukowski S, Suski T and Porowski S 2000 Electron spin resonance of erbium in gallium nitride *Solid State Commun.* **114** 39–42

[71] David A and Grundmann M J 2010 Droop in InGaN light-emitting diodes: A differential carrier lifetime analysis *Appl. Phys. Lett.* **96** 103504

[72] Neugebauer J and Van de Walle C G 1995 Hydrogen in GaN: Novel Aspects of a Common Impurity *Phys. Rev. Lett.* **75** 4452–5

[73] Brandt M S, Johnson N M, Singh R and Moustakas T D 1994 Hydrogenation of p-type gallium nitride **64** 2264–6

[74] Götz W, Johnson N M, Walker J, Bour D P, Amano H and Akasaki I 1995 Hydrogen passivation of Mg acceptors in GaN grown by metalorganic chemical vapor deposition *Appl. Phys. Lett.* **67** 2666

[75] Suihkonen S, Pimputkar S, Speck J S and Nakamura S 2016 Infrared absorption of hydrogen-related defects in ammonothermal GaN *Appl. Phys. Lett.* **108** 202105

[76] Lyons J L, Alkauskas A, Janotti A and Van de Walle C G 2015 First-principles theory of acceptors in nitride semiconductors *Phys. Status Solidi Basic Res.* **252** 900–8

[77] Sun Y Y, Abtew T A, Zhang P and Zhang S B 2014 Anisotropic polaron localization and spontaneous symmetry breaking: Comparison of cation-site acceptors in GaN and ZnO *Phys. Rev. B* **90** 165301

[78] Kunzer M, Kaufmann U, Maier K, Schneider J, Herres N, Akasaki I and Amano H 1993 ODMR Studies of MOVPE-Grown GaN Epitaxial Layers *Mater. Sci. Forum* **143**–**147** 87–92

[79] Kennedy T A, Glaser E R, Freitas J A, Carlos W E, Khan M A and Wickenden D K 1995 Native defects and dopants in gan studied through photoluminescence and optically detected magnetic resonance *J. Electron. Mater.* **24** 219–23

[80] Glaser E R, Kennedy T A, Doverspike K, Rowland L B, Gaskill D K, Freitas J A, Asif Khan M, Olson D T, Kuznia J N and Wickenden D K 1995 Optically detected magnetic resonance of GaN films grown by organometallic chemical-vapor deposition *Phys. Rev. B* **51** 13326–36

[81] Alves H, Leiter F, Pfisterer D, Hofmann D M, Meyer B K, Einfeld S, Heinke H and Hommel D 2003 Mg in GaN: the structure of the acceptor and the electrical activity *Phys. status solidi* **0** 1770–82

[82] Lyons J L, Janotti A and Van de Walle C G 2012 Shallow versus Deep Nature of Mg Acceptors in Nitride Semiconductors *Phys. Rev. Lett.* **108** 156403

[83] Glaser E R, Murthy M, Freitas J A, Storm D F, Zhou L and Smith D J 2007 Optical and magnetic resonance studies of Mg-doped GaN homoepitaxial layers grown by molecular beam epitaxy *Phys. B Condens. Matter* **401**–**402** 327–30

[84] Aliev G N, Zeng S, Davies J J, Wolverson D, Bingham S J, Parbrook P J and Wang T 2005 Nature of acceptor states in magnesium-doped gallium nitride *Phys. Rev. B* **71** 195204

[85] Freitas J A, Culbertson J C, Mahadik N A, Sochacki T, Iwinska M and Bockowski M S 2016 HVPE GaN wafers with improved crystalline and electrical properties *J. Cryst. Growth* **456** 113–20

[86] Reshchikov M A, Xie J, He L, Gu X, Moon Y T, Fu Y and Morkoç H 2005 Effect of potential fluctuations on photoluminescence in Mg-doped GaN *Phys. status solidi* **2** 2761–4

[87] Zvanut M E, Dashdorj J, Sunay U R, Leach J H and Udwary K 2016 Effect of local fields on the Mg acceptor in GaN films and GaN substrates *J. Appl. Phys.* **120** 135702

[88] Weil J A and Bolton J R 2010 *Electron Paramagnetic Resonance: Elementary Theory and Practical Applications* vol 22 (Hoboken: John Wiley & Sons, Inc.)

[89] Blair D P and Sydenham P H 1975 Phase sensitive detection as a means to recover signals buried in noise *J. Phys. E.* **8** 621–7

[90] Elliott R and Stevens K 1952 The theory of the magnetic properties of rare earth salts: cerium ethyl sulphate *Proc. R. Soc. London. Ser. A. Math. Phys. Sci.* **215** 437–53

[91] Abragam A and Bleaney B (Brebis) 2012 *Electron paramagnetic resonance of transition ions* (Oxford University Press)

[92] Gerloch M and Miller J R 2007 Covalence and the Orbital Reduction Factor, k , in Magnetochemistry *Progress in Inorganic Chemistry* vol 10 pp 1–47

[93] Wertz J E and Bolton J R 1986 Biological Applications of Electron Spin Resonance *Electron Spin Resonance* (Dordrecht: Springer Netherlands) pp 378–90

[94] Farach C P P and H A 1964 Line Shapes in Electron Spin Resonance Spectra *J. Chem. Phys.* **41** 949–59

[95] Poole C P 1967 *Electron spin resonance : a comprehensive treatise on experimental techniques* (Wiley)

[96] Malyshev A V, Merkulov I A and Rodina A V 1998 Effective Mass Calculation of the Shallow Acceptor Ground State g-Factor for A3B5 Semiconductors *Phys. status solidi* **210** 865–8

[97] Tompkins R P, Walsh T A, Derenge M A, Kirchner K W, Zhou S, Nguyen C B, Jones K A, Mulholland G, Metzger R, Leach J H, Suvarna P, Tungare M and Shahedipour-Sandvik F (Shadi) 2013 HVPE GaN for high power electronic Schottky diodes *Solid. State. Electron.* **79** 238–43

[98] Mola M, Hill S, Goy P and Gross M 2000 Instrumentation for millimeter-wave magnetoelectrodynamic investigations of low-dimensional conductors and superconductors *Rev. Sci. Instrum.* **71** 186–200

[99] Łucznik B, Pastuszka B, Grzegory I, Boćkowski M, Kamler G, Domagała J, Nowak G, Prystawko P, Krukowski S and Porowski S 2006 Crystallization of free standing bulk GaN by HVPE *Phys. Status Solidi Curr. Top. Solid State Phys.* **3** 1453–6

[100] Wertz J E and Bolton J R 1986 *Electron Spin Resonance* (Dordrecht: Springer Netherlands)

[101] Stępniewski R, Wysmołek A, Potemski M, Pakuła K, Baranowski J M, Grzegory I, Porowski S, Martinez G and Wyder P 2003 Fine Structure of Effective Mass Acceptors in Gallium Nitride *Phys. Rev. Lett.* **91** 226404

[102] Misra P, Behn U, Brandt O, Grahn H T, Imer B, Nakamura S, DenBaars S P and Speck J S 2006 Polarization anisotropy in GaN films for different nonpolar orientations studied by polarized photoreflectance spectroscopy *Appl. Phys. Lett.* **88** 161920

[103] Ham F S 1965 Dynamical Jahn-Teller Effect in Paramagnetic Resonance Spectra: Orbital Reduction Factors and Partial Quenching of Spin-Orbit Interaction *Phys. Rev.* **138** A1727–40

[104] Aasa R and Vänngård tore 1975 EPR signal intensity and powder shapes: A reexamination *J. Magn. Reson.* **19** 308–15

[105] Pilbrow J . 1984 Lineshapes in frequency-swept and field-swept epr for spin 1/2* *J. Magn. Reson.* **58** 186–203

[106] Cao Y J and Wu Q H 2013 Teaching Genetic Algorithm Using Matlab *Int. J. Electr. Eng. Educ.* **36** 139–53

[107] Zvanut M E, Uprety Y, Dashdorj J, Moseley M and Alan Doolittle W 2011 Passivation and activation of Mg acceptors in heavily doped GaN *J. Appl. Phys.* **110** 044508

[108] Look D C, Jones R L, Sun X L, Brillson L J, Ager J W, Park S S, Han J H, Molnar R J and Maslar J E 2002 Electrical and optical properties of GaN/Al_2O_3 interfaces *J. Phys. Condens. Matter* **14** 13337–44

[109] Hsu J W P, Lang D V., Richter S, Kleiman R N, Sergent A M, Look D C and Molnar R J 2001 Impurity band in the interfacial region of GaN films grown by hydride vapor phase epitaxy *J. Electron. Mater.* **30** 115–22

[110] Sunay U R, Zvanut M E and Allerman A A 2015 Reduction in the Number of Mg Acceptors with Al Concentration in AlxGa1−xN *J. Electron. Mater.* **44** 4139–43

[111] Kunzer M, Baur J, Kaufmann U, Schneider J, Amano H and Akasaki I 1997 Properties of Mg and Zn acceptors in MOVPE GaN as studied by optically detected magnetic resonance *Solid. State. Electron.* **41** 189–93

[112] Angerer H, Brunner D, Freudenberg F, Ambacher O, Stutzmann M, Höpler R, Metzger T, Born E, Dollinger G, Bergmaier A, Karsch S and Körner H-J 1997 Determination of the Al mole fraction and the band gap bowing of epitaxial AlxGa1−xN films *Appl. Phys. Lett.* **71** 1504–6

[113] Van de Walle C G 2003 Effects of impurities on the lattice parameters of GaN *Phys. Rev. B - Condens. Matter Mater. Phys.* **68** 1–5

[114] Zajac M, Kucharski R, Grabianska K, Gwardys-Bak A, Puchalski A, Wasik D, Litwin-Staszewska E, Piotrzkowski R, Z Domagala J and Bockowski M 2018 Basic ammonothermal growth of Gallium Nitride – State of the art, challenges, perspectives *Prog. Cryst. Growth Charact. Mater.* **64** 63–74

[115] Darakchieva V, Paskova T, Paskov P P, Monemar B, Ashkenov N and Schubert M 2003 Residual strain in HVPE GaN free-standing and re-grown homoepitaxial layers *Phys. Status Solidi Appl. Res.* **195** 516–22

[116] Nehrkorn J, Schnegg A, Holldack K and Stoll S 2015 General magnetic transition dipole moments for electron paramagnetic resonance *Phys. Rev. Lett.* **114** 5–9

[117] Patel J L, Nicholls J E and Davies J J 1981 Optically detected magnetic resonance of two shallow acceptor centres in cadmium sulphide *J. Phys. C Solid State Phys.* **14** 1339–49

[118] Davydov V Y, Averkiev N S, Goncharuk I N, Nelson D K, Nikitina I P, Polkovnikov A S, Smirnov A N, Jacobson M A and Semchinova O K 1997 Raman and photoluminescence studies of biaxial strain in GaN epitaxial layers grown on 6H–SiC *J. Appl. Phys.* **82** 5097–102

[119] Ghosh S, Waltereit P, Brandt O, Grahn H T and Ploog K H 2002 Electronic band structure of wurtzite GaN under biaxial strain in the M plane investigated with photoreflectance spectroscopy *Phys. Rev. B - Condens. Matter Mater. Phys.* **65** 1–7

[120] STONEHAM A M 1969 Shapes of Inhomogeneously Broadened Resonance Lines in Solids *Rev. Mod. Phys.* **41** 82–108

[121] Hearshen D ., Hagen W ., Sands R ., Grande H ., Crespi H ., Gunsalus I . and Dunham W . 1986 An analysis of g strain in the EPR of two [2Fe□2S] ferredoxins. Evidence for a protein rigidity model *J. Magn. Reson.* **69** 440–59

[122] Davies J J 2013 Magnetic resonance and the structure of magnesium acceptors in gallium nitride *Phys. Rev. B - Condens. Matter Mater. Phys.* **87** 1–5

[123] Orbach R 1961 Spin-lattice relaxation in rare-earth salts *Proc. R. Soc. London. Ser. A. Math. Phys. Sci.* **264** 458–84

[124] Bersuker I 2006 *The Jahn–Teller Effect* (Cambridge: Cambridge University Press)

[125] Independent S C, Interacting S C, Components S and Combination I N 1937 Stability of polyatomic molecules in degenerate electronic states - I—Orbital degeneracy *Proc. R. Soc. London. Ser. A - Math. Phys. Sci.* **161** 220–35

[126] Independent S C, Interacting S C, Components S and Combination I N 1937 Stability of polyatomic molecules in degenerate electronic states - I—Orbital degeneracy *Proc. R. Soc. London. Ser. A - Math. Phys. Sci.* **161** 220–35

[127] Watkins G D 1975 Defects in irradiated silicon: EPR and electron-nuclear double resonance of interstitial boron *Phys. Rev. B* **12** 5824–39

[128] Gutowsky H S and Saika A 1953 Dissociation, chemical exchange, and the proton magnetic resonance in some aqueous electrolytes *J. Chem. Phys.* **21** 1688–94

[129] Chase L L 1970 Microwave-Optical Double Resonance of the Metastable 4f6 5d Level of Eu2+ in the Fluorite Lattices *Phys. Rev. B* **2** 2308–18

[130] Boatner L A, Reynolds R W, Chen Y and Abraham M M 1977 Static, quasistatic, and quasidynamic Jahn-Teller effect in the EPR spectra of Ag2+ in SrO, CaO, and MgO *Phys. Rev. B* **16** 86–106

[131] Stevens K W H 1953 On the magnetic properties of covalent XY 6 complexes *Proc. R. Soc. London. Ser. A. Math. Phys. Sci.* **219** 542–55

[132] Thiering G and Gali A 2017 Ab initio calculation of spin-orbit coupling for an NV center in diamond exhibiting dynamic Jahn-Teller effect *Phys. Rev. B* **96** 1–6

[133] Snow R L and Bills J L 1975 A simple illustration of the SCF-LCAO-MO method *J. Chem. Educ.* **52** 506

APPENDIX

Calculating EPR Parameters From Hamiltonian Parameters For Mg^0

This section is intended to outline the procedure for calculating the g-factor anisotropy and intensity for a given EPR defect with a specified Hamiltonian. Computational calculations of EPR transition characteristics are straightforward when given a Hamiltonian and basis set for a S = ½ spin system [88,117]. Firstly, the Hamiltonian is separated into a magnetic field dependent component and independent component, i.e. $H = H_o + H_B$, here H_B contains the magnetic field dependent interactions. In this work, many of the Mg EPR characteristics can be well described if H_o has the terms

$$H_o = \Delta_z\left(\hat{L}_z^2 - L(L+1)/3\right) + \Delta_x\left(\hat{L}_x^2 - L(L+1)/3\right) + \lambda \boldsymbol{L}\cdot\boldsymbol{S} \qquad \text{(A.1)}$$

Where the second term is a crystal field in the x-direction. At resonance, the Zeeman energy splitting is very small compared to the energy terms in H_o (0.04 meV at 10 GHz). Therefore, H_B is taken as a perturbation on H_o. The magnetic-independent Hamiltonian H_o is diagonalized in a given basis set – in this work that basis set is atomic 2p orbitals. At this point, an analytical diagonalization is not trivial. Instead, numerical diagonalization was completed via MATLAB using explicit values for Δ_z, Δ_x, and λ. If the elements of the matrix are of different orders of magnitude then, depending on the diagonalization algorithm, the eigenvector solution can be unstable and higher precision is required. The method used to find the matrix equivalent operators for **L** and **S** is given in a typical

quantum mechanics textbook. The lowest energy state, now referred to as the ground state, should correspond to two distinct quantum states $|i\rangle$ and $|j\rangle$., i.e. be degenerate. This degeneracy will be broken by the magnetic field-dependent term H_B which is expressed in Eq. 2.5 (b). The calculated EPR g-factors are expressed explicitly as

$$g_x = 2\left|\langle i|\left(g_e\hat{S}_x + g_l\hat{L}_x\right)|j\rangle\right| \quad \text{(A.2a)}$$

$$g_y = 2\left|\langle i|\left(g_e\hat{S}_y + g_l\hat{L}_y\right)|j\rangle\right| \quad \text{(A.2b)}$$

$$g_z = 2\left|\langle i|\left(g_e\hat{S}_z + g_l\hat{L}_z\right)|i\rangle\right| \quad \text{(A.2c)}$$

The Mg-related EPR signal has axial symmetry about the c-axis, so $g_x = g_y = g_\perp$ and $g_z = g_\parallel$.

The next step is to calculate an EPR transition intensity by applying Eq 2.6. The most computationally expensive component of calculating an EPR transition intensity comes from the first term of Eq. 2.10

$$|\langle i|\boldsymbol{H}_{mw}|f\rangle|^2 \quad \text{(A.3)}$$

For a given angle θ_i between the static magnetic field $\boldsymbol{B}$ and the g-factor defect coordinates, the mixing between the ground state and excited states changes. For the measurements in this work, the sample is rotated in a plane containing the c-axis and can now explicitly express Eq. 2.6 as

$$\widehat{H}_B = \mu_B B\left(\cos(\theta_i)\left[\hat{S}_z g_e + g_l \hat{L}_z\right] + \sin(\theta_i)\left[\hat{S}_x g_e + g_l \hat{L}_x\right]\right) \tag{A.4}$$

To do this we must first perform first order degenerate wavefunction corrections on the ground states $|i\rangle$ and $|j\rangle$, i.e. diagonalize the matrix

$$\widehat{H}_B = \begin{pmatrix} \langle i|\widehat{H}_B|i\rangle & \langle j|\widehat{H}_B|i\rangle \\ \langle i|\widehat{H}_B|j\rangle & \langle j|\widehat{H}_B|j\rangle \end{pmatrix} \tag{A.5}$$

and use the new wavefunctions $|i'\rangle$ and $|j'\rangle$ which are linear combinations of $|i\rangle$ and $|j\rangle$. By performing this diagonalization on the degenerate states, we are able to confidently perform non-degenerate perturbation without concern of a divergent correction term.

Next, we need to find the magnetic field B_o at resonance. To first order, this is the linear response term calculated from "traditional EPR" analysis $B_o = \frac{hv}{\mu 0_B g}$, but higher order correction terms were also inspected to confirm that they are negligible. The change in energy for the states $|i'\rangle$ and $|j'\rangle$ from the applied magnetic field is

$$E_n = E_n^{(0)} + E_n^{(1)} + E_n^{(2)} + \cdots \tag{A.6a}$$

$$E_n^{(1)} = \langle n|\widehat{H}_B|n\rangle \tag{A.6b}$$

$$E_n^{(2)} = \sum_{m \neq n} \frac{\left|\langle m^{(0)}|\widehat{H}_B|n^{(0)}\rangle\right|^2}{E_n^{(0)} - E_m^{(0)}} \tag{A.6.c}$$

where $E_n^{(k)}$ is the kth order perturbation term of the nth wavefunction. Additionally, the order of the correction term *k* will correspond to the polynomial order of the magnetic field B. At resonance, the energy difference between the two spin states must be equal to the microwave photon energy hυ or

$$\Delta E = h\nu = E_{i'} - E_{j'} = \left(E_{i'}^{(1)} - E_{j'}^{(1)}\right) + \left(E_{i'}^{(2)} - E_{j'}^{(2)}\right) + \cdots \quad \text{(A.7a)}$$

$$h\nu = C_1 B + C_2 B^2 + C_3 B^3 + \cdots \quad \text{(A.7b)}$$

where C_k is the *k*th order non-magnetic field component energy difference between states$|i'\rangle$ and $|j'\rangle$. These higher order terms represent the paramagnetic center's non-linear response to an external magnetic field and, typically, account for less than a 0.1 mT change in the resonant position. Now, for a given microwave frequency υ, we can solve the polynomial Eq. A.7b for the resonant magnetic field B_o.

We can now apply the perturbation of H_B to the wavefunctions $|i'\rangle$ and $|j'\rangle$ to obtain correction terms to the wavefunction

$$|i''\rangle = |i'\rangle^{(0)} + |i'\rangle^{(1)} + |i'\rangle^{(2)} + \cdots \quad \text{(A.8a)}$$

$$|j''\rangle = |i'\rangle^{(0)} + |i'\rangle^{(1)} + |i'\rangle^{(2)} + \cdots \quad \text{(A.8b)}$$

The last step in determining the intensity, is to compute Eq. 2.10 with the perturbation corrected wavefunctions.

As always, more complexity can be added to each of these steps. For example, hybridization of orbitals can be modeled by a linear combination of atomic orbitals (LCAO). Instead of exact diagonalization to determine eigen-states and eigen-energies, a self-consistent field (SCF) method can be applied [133]. For these methods to be applied, more information about hyperfine interactions must be determined.